GeoScienceWorld
Lithosphere
Volume 2023, Article ID 8711959, 24 pages
https://doi.org/10.2113/2023/8711959

Lithosphere

Research Article

Investigation into the Multistage Mechanical Damage Behavior of Columnar Jointed Basalts with Different Meso-Constitutive Relations and Model Sizes

Yongyi Wang,[1] Bin Gong,[2] Xiaoyu Yang,[3] and Chun'an Tang[1]

[1]*State Key Laboratory of Coastal & Offshore Engineering, Dalian University of Technology, Dalian 116024, China*
[2]*Department of Civil and Environmental Engineering, Brunel University London, London UB8 3PH, UK*
[3]*School of Civil Engineering, Chongqing Jiaotong University, Chongqing 400074, China*

Correspondence should be addressed to Bin Gong; bin.gong@brunel.ac.uk

Received 3 October 2022; Revised 15 December 2022; Accepted 24 January 2023; Published 20 October 2023

Academic Editor: Min-Te Chen

The mechanical characteristics of columnar jointed basalts (CJBs) are generally considered to be subject to size effects. They display complex mechanical behaviors under lateral pressure, which may be related to the variation in the rock's mesoproperties. In this study, many nonuniform CJB models with various rock meso-constitutive relations and model sizes were established, and their influences on the strength and deformation properties, multistage mechanical damage behavior, and acoustic emission characteristics of CJBs were investigated. The results show that, as the residual strength coefficient increases, the compressive strength of CJBs rises, and the equivalent deformation modulus of CJBs decreases or increases slightly; with an increase in the model size, the compressive strength slightly decreases at first and then varies moderately, and the equivalent deformation modulus shows a fluctuating trend. Furthermore, the macro stress–strain relationships can be divided into different stages according to the corresponding damage behaviors. The strains and energy accumulations before peak stress was reached were further analyzed. The results greatly improve our understanding of the collapse process of CJBs and the instability precursors of related structures.

1. Introduction

Columnar jointed basalts (CJBs) are rock masses with regular fractures produced through magma cooling. They are distributed widely around the world and can be found in Northern Ireland, Scotland, Brazil, China, Siberia, Mexico, India, Australia, the United States, and so on [1–5]. They are characterized by regular hexagonal prisms or other irregular prisms, and the mechanical properties are generally considered to be affected by size effects [6]. Additionally, they display various strength or deformation characteristics with or without lateral pressure, which may be related to the variation in the rock's meso properties. In recent decades, CJBs have been encountered in numerous engineering projects in China, including the Hunan Town, Guandi, Xiluodu, Tongjiezi, Ertan, Baihetan, Wudongde, Jinanqiao hydropower stations, and so on [7–10]. Some field photographs [11, 12] of CJBs are shown in Figure 1.

Many scholars [8, 13–15] have investigated the anisotropy, size effect, and lateral pressure influence of CJBs. Although valuable results have been obtained in field tests involving CJBs, the environments of engineered rock structures in field tests are often affected by many factors, and rock specimens are affected by disturbances. The creep characteristics of columnar jointed rock masses (CJRMs) in the dam zone were studied by Wei et al. [13], but the effects of rock meso property variation were difficult to identify when using their research method. Furthermore, due to limitations in terms of experimental equipment and techniques, it is very difficult to carry out large sample tests. For CJBs at the Baihetan hydropower station, a drilling experiment was conducted in the excavation damage zone

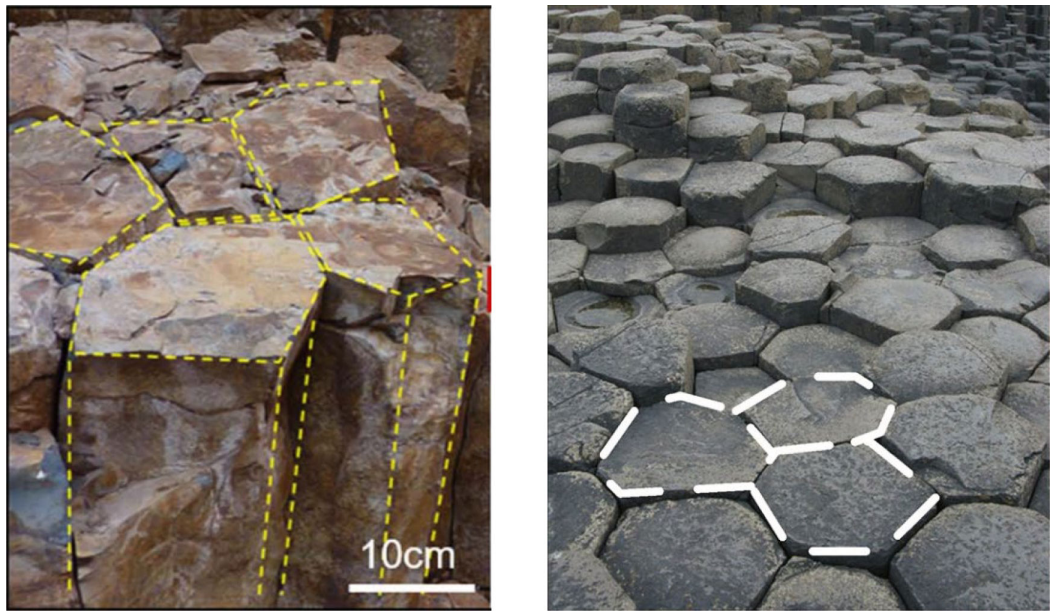

Figure 1: The observed CJBs in the field: (a) Baihetan hydroelectric station, China [11]; (b) Giant's Causeway, Northern Ireland [12].

(EDZ) as well as in undisturbed rocks by Sun et al. [14]. Nevertheless, the samples were susceptible to borehole disturbance. Based on an in situ, large-scale blasting test, the release laws of the acoustic emissions (AEs) were analyzed by Xiang et al. [8], and the unloading processes and relaxation mechanisms of CJBs were revealed. Zhang et al. [4] performed a series of field tests to investigate the EDZ of CJRMs that involved monitoring ultrasonic *P* waves. Jiang et al. [15] conducted a crack observation and time-dependent failure experiment on CJRMs, but in their research, the damage evolution at different stages was difficult to comprehensively display. Dou et al. [2] carried out a field test to investigate consolidation grouting in the CJB foundation of dams. Nevertheless, in the above studies, the rock mass occurrence environment was too complex for in situ tests, and it is difficult to take the influence of rock's mesoproperties into account in systematic research.

In physical laboratory tests on CJBs (or CJRMs), some useful results reflecting their mechanical properties have been obtained [1, 11, 12]. However, there are still difficulties when considering the mechanical parameters of actual joint surfaces in physical laboratory tests. Additionally, when there are many experimental scheme configurations and specimens, these tests can become time-consuming and uneconomical. Ji et al. [11] performed conventional triaxial compression tests to investigate the anisotropic strength and deformation behaviors of CJRMs in a confined state, but the effects of variations in rock's mesoproperties under confining pressure remain unclear. Zhang et al. [16] conducted a cyclic triaxial loading–unloading experiment to reveal the anisotropic behavior of CJRMs. However, due to the limitations of the laboratory equipment, the size effect of specimens was not studied fully. Uniaxial and triaxial compression experiments were carried out by Lu et al. [12] to determine the fracture mechanisms of CJRMs. Nevertheless, the changes in the rock's mesoproperties during the experiment were generally difficult to observe in their research. The failure mechanism, stress–strain curve, and peak strengths of CJRMs were investigated by Zhu et al. [17]. However, the progressive damage behaviors of specimens were not analyzed in their research. Laboratory triaxial seepage tests were conducted by He et al. [7, 18] to clarify the seepage features of CJRMs under different stress states. Xu et al. [1] carried out unloading experiments on similar material specimens, and acoustic wave data were monitored. In the above studies, the influence of the size effect was not considered properly, and the damage evolution of CJBs with different rock's mesoproperties under lateral pressure is not yet fully understood.

In the numerical simulation of CJBs (or CJRMs), insightful findings have been obtained [4, 19, 20]. However, there are few systematic studies on the effects of model size, rock meso-constitutive relations, and model boundaries on the damage behavior of CJBs. Meng et al. [6] conducted a uniform simulation to reveal the influence of the columnar joint set on the mechanical parameters of rocks, but the damage process of CJRMs was not considered. On the basis of the three-dimensional (3D) finite difference method, an elastoplastic numerical model of CJRMs was proposed by Yu et al. [19], and the excavation-induced relaxation zones of the diversion tunnel were reproduced. However, the size effect of CJRMs was not taken into account in their research. Wang et al. [21] performed a series of simulations involving the cracking mechanisms and energy release laws of CJRMs using digital image correlation (DIC) and the rock failure process analysis (RFPA) method. Nevertheless, the influence of rock meso-constitutive relations on the

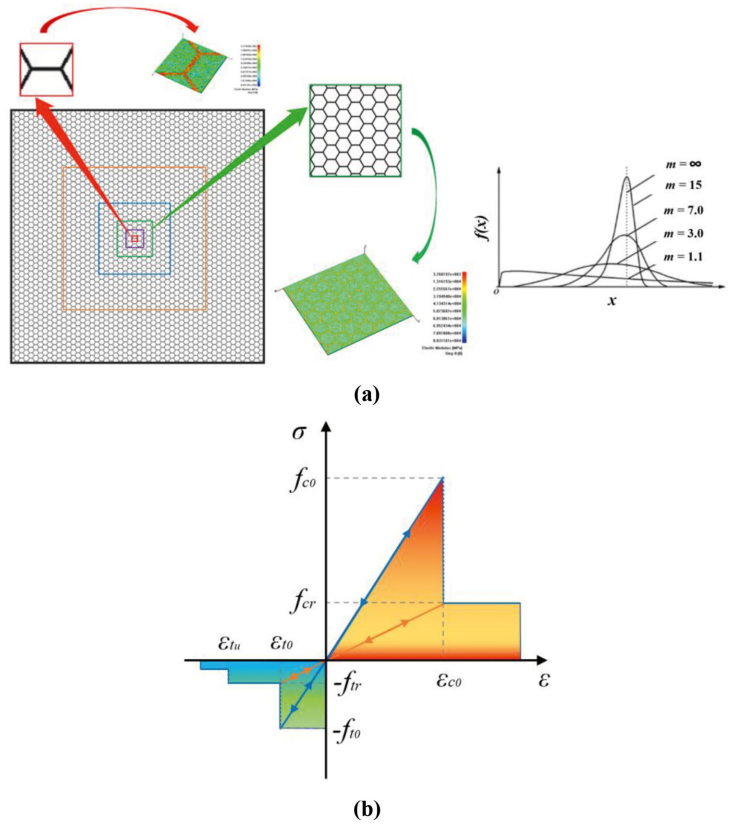

FIGURE 2: (a) The process of transforming a digital image into a computable heterogeneous model; (b) the stress–strain relationships of an element subject to uniaxial stress (Note: m is the heterogeneity coefficient [24]).

damage characteristics of CJRMs under lateral pressure remains unclear. A 3D numerical analysis was conducted by Zhang et al. [4] to analyze the unloading-induced damage mechanisms of CJRMs. Additionally, a numerical simulation was performed by Zhang et al. [22] to investigate the mechanism of stress–structural collapse in CJRMs under high-stress environments. Li et al. [23] investigated the transient thermoelastic fracture problems of rocks using a high-accuracy numerical manifold method. In the above studies, the damage evolution of CJRMs affected by rock's mesoproperties and model sizes was not systematically studied. Cheng et al. [3] investigated the flow and permeability properties of irregular CJRMs numerically. However, the above studies did not comprehensively consider the influence of the sizes of established numerical models, rock meso-constitutive relations, and model boundaries on the damage processes and AE energy evolutions of CJBs.

In this paper, to analyze the multistage mechanical damage behavior of CJBs with different rock meso-constitutive relations and model sizes under lateral pressure, continuum mechanics and damage mechanics were applied, digital images of CJB specimens were transformed into corresponding heterogeneous models by DIC, and a series of simulations were conducted. Then, the numerical tests were compared to the physical tests to verify the rationality and reliability of our results. Additionally, the mechanical damage evolutions of CJBs under lateral pressure were reproduced. The influence of rock meso-constitutive relations, model sizes, and model boundaries on the multistage mechanical damage behavior of CJBs was also investigated.

2. Method

2.1. Basic Principles. The main advantages of the RFPA approach are that there are no assumptions about the location where new fractures will initiate or the way in which newly formed or existing fractures will develop [24–26]. The effectiveness of this method has been verified by many benchmark studies [27–29]. This approach has been used to assess slope safety, tunnel stability, and the mechanical properties of rocks in many studies [30–33]. Thus, it is an effective method for modeling rock mechanics. In order to build up the computable numerical model, a digital image consisting of square pixels is transformed into the necessary node coordinates and element materials by DIC. Based on gray threshold segmentation, each element corresponding to a pixel is assigned joint or rock material properties. According to these principles, the schematic diagram for transforming a digital image into a heterogeneous numerical model is presented in Figure 2(a). At the same time, the stress–strain relationship of elements subject to a uniaxial stress state is depicted in Figure 2(b). According to Mazars and Pijaudier-Cabot [34], the constitutive relation under uniaxial stress can be extended to a 3D stress state.

Table 1: The physico-mechanical properties used in the simulation.

Material type	Heterogeneity index	Elastic modulus (GPa)	Uniaxial compressive strength (MPa)	Poisson ratio	Friction angle (°)	Ratio of compression to tension	Coefficient of residual strength
Rock	5	60	120	0.2	56.15	10	0.1
Joint	5	15	30	0.25	36	10	1

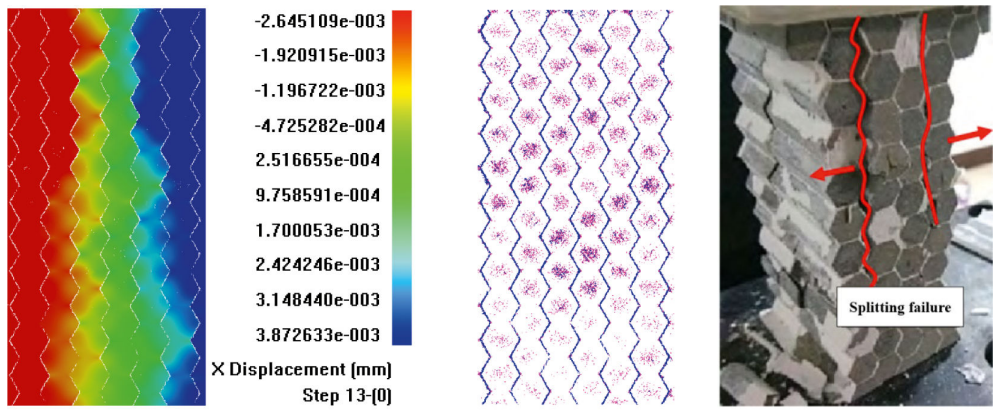

Figure 3: Comparison between numerical and experimental results: (a) the numerical x-direction displacement contour; (b) the numerical AE diagram; (c) the experimental failure mode [35].

2.2. Benchmark. The experimental test by Ke et al. [35] was adopted to examine the established computational method. They made columns by mixing cement, fine sand, water, and water reducer at a mass ratio of 1.000:0.500:0.350:0.002. A hexagonal prism with a section diameter and length of 10 and 50 mm, respectively, was selected to simulate the actual column. A white cement slurry with a water–cement ratio of 0.400:1.000 was used to bond columns, which simulated the joint surface. The rock mass specimens were regular 50 × 50 mm quadrangular prism samples with a height of 100 mm. The experiment was carried out using a CSS-3940YJ rock mechanics servo testing machine. A loading method with a constant displacement rate of 0.05 mm/min was adopted until the failure of the specimens.

The plane strain assumption was adopted. The size of the rectangular specimens was 50 × 50 × 100 mm, and the diameter of the hexagonal prisms within the samples was 10 mm. The direction I orthogonal to the column axis was considered. The finite element model was established by processing the digital image with DIC. Specifically, the identification of joints and matrices was conducted by DIC. The joints were simulated by the elements with relatively low strengths and elastic modului. After recognizing joint elements and matrix elements using threshold segmentation, the corresponding material parameters were assigned, respectively. The physico-mechanical parameter values from the literature [1, 6, 13, 15, 16] are presented in Table 1.

Because of the material heterogeneity, the elastic moduli or strengths of adjacent elements are not equal, and their distribution was assumed to obey the Weibull distribution [36] in this study. Through this method, the heterogeneity of the rock mass was considered. The shape parameter of the Weibull distribution is called the heterogeneity index. The larger the homogeneity index, the more homogeneous the rock material, and vice versa. A displacement load ratio of 0.005 mm/step was applied to the top surface of the samples, and the bottom was fixed along the normal direction. The numerical results were compared to the results of the physical experiments, as displayed in Figure 3. Note that the blue dots in the AE diagrams of the numerical tests represent the tensile failures, and the red dots represent the compressive failures. It can be seen in Figure 3 that the numerical results agree with the experimental results satisfactorily.

2.3. Model Configuration. In terms of model size, seven cases were considered, that is, 0.5 × 0.5 m, 1.0 × 1.0 m, 2.0 × 2.0 m, 3.0 × 3.0 m, 4.0 × 4.0 m, 6.0 × 6.0 m, and 8.0 × 8.0 m. The column diameter inside the specimen was 20 cm. The size of the inner finite elements kept the same. For instance, the element number of the 8 × 8 m sample was 4,326,400. The residual strength coefficient (RSC) of the CJBs was set to 0.1, 0.5, and 1 sequentially, as can be seen in Figure 4.

The other physical and mechanical parameters of the rock and joint are the same as those listed in Table 1. In terms of the nonuniformity of the mechanical properties of the rock and joint, it is assumed that they obey the given Weibull distribution, and the heterogeneity index is taken to be 5. Figure 2(a) shows a locally enlarged

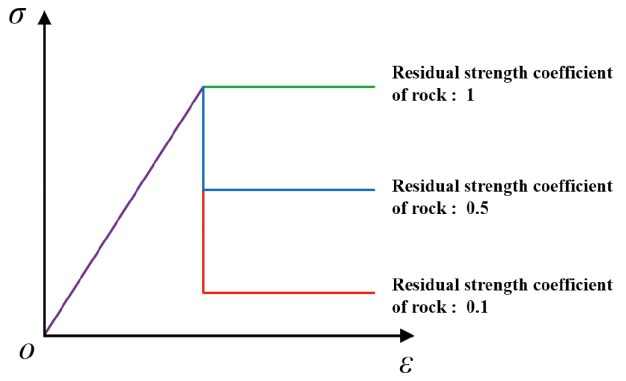

Figure 4: Rock meso-constitutive relations with different residual strength coefficients.

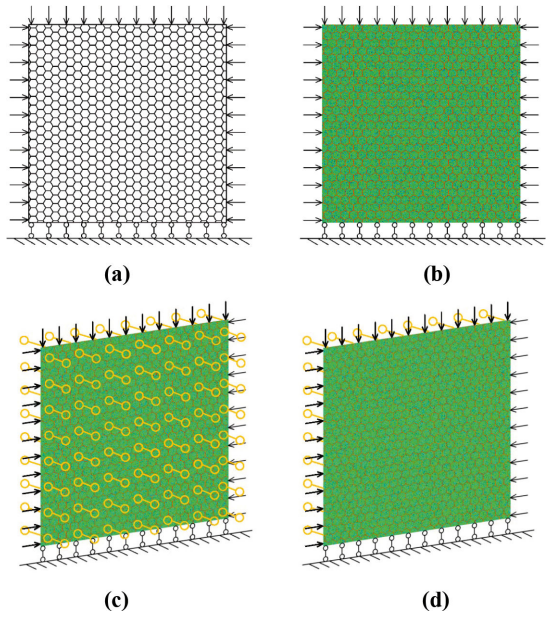

Figure 5: Model setting under lateral pressure: (a) direction Ⅰ of the digital image; (b) the finite element model along direction Ⅰ Ⅰ; (c) the plane strain case; (d) the case between plane stress and plane strain.

diagram of a specimen. Figures 5(a) and 5(b) present the typical setting and boundary conditions of a CJB specimen under lateral pressure. Note that directions I and II are considered. For the plane strain case, the displacement of the model plane is constrained to 0 m along the positive and negative normal directions, in the same manner as the internal surrounding rocks along a tunnel axis, as can be seen in Figure 5(c). For the case between plane stress and plane strain, the displacement of the model plane is constrained to 0 m along the positive normal direction, in the same manner as rocks near a tunnel wall, as can be seen in Figure 5(d). The principle of transforming a digital image of CJSs into a finite element mesh can be seen in section 2.1. The lateral pressures of 4 and 8 MPa are considered. Displacement-controlled loading is applied to the upper surface of the model vertically until the macrofailure of the sample.

3. Results and Analysis

3.1. The Effects of Rock Meso-Constitutive Relations and Model Size under Lateral Pressure

3.1.1. The Plane Strain Case

3.1.1.1. Compressive Strength. In Figures 6(a)–6(c), it can be seen that when the RSC = 1 and the lateral pressure = 4 MPa, the critical value of the size effect for the compressive strength (CS) of CJBs is 4 m, while in the other cases, the critical value of the size effect for the CS of CJBs is around 6 m. Meanwhile, the CS of CJBs grows with an increase in the rock RSC, and the CS of CJBs increases significantly when the lateral pressure rises from 4 to 8 MPa. In particular, for CJBs with model sizes of 0.5–4 m, the growth ratio of the CS of CJBs is in line with the growth in lateral pressure.

Figures 6(d)–6(f) show the CSs of the CJBs with different rock RSCs and model sizes, from which it can be seen that with a growth in model size, the CS first slightly decreases and then changes moderately. At the same time, the critical value of the size effect for the CS of CJBs is about 6 m, and the CS of CJBs rises with a growth in the rock RSC. Additionally, except for individual cases, the CS of CJBs along direction Ⅰ Ⅰ is higher than that along direction I.

3.1.1.2. Equivalent Deformation Modulus. Figures 7(a)–7(c) show the equivalent deformation moduli (EDMs) of the CJBs with different RSCs (i.e., 0.1, 0.5, and 1.0) and model sizes. From the perspective of model size, the EDM fluctuates slightly with a growth in the model size. At the same time, with an increase in the RSC, the EDM of CJBs decreases slightly. In terms of lateral pressure, the EDM of CJBs grows slightly with an increase in lateral pressure.

In Figures 7(d)–7(f), we can see that with an increase in model size, the EDM fluctuates, but the variation range is relatively small. For instance, for the CJBs with a rock RSC of 0.1 along direction I perpendicular to the column axis, the ratio of the maximum value to the minimum value of the EDMs is 1.068; for the CJBs with a rock RSC of 1.0 along direction II perpendicular to the column axis, the ratio of the maximum value to the minimum value of the EDMs is 1.161. Furthermore, with a growth in the rock RSC, the EDMs of CJBs change slightly, and except for a few special cases, the EDM along direction II perpendicular to the column axis is slightly larger than that along direction I.

3.1.2. Model Boundaries. In Figure 8, case Ⅰ represents the case between plane stress and plane strain, and case II represents the plane strain case. As can be seen in Figure 8(a), along direction I perpendicular to the column axis, with an increase in the model size, the CS of CJBs drops at first and then changes moderately,

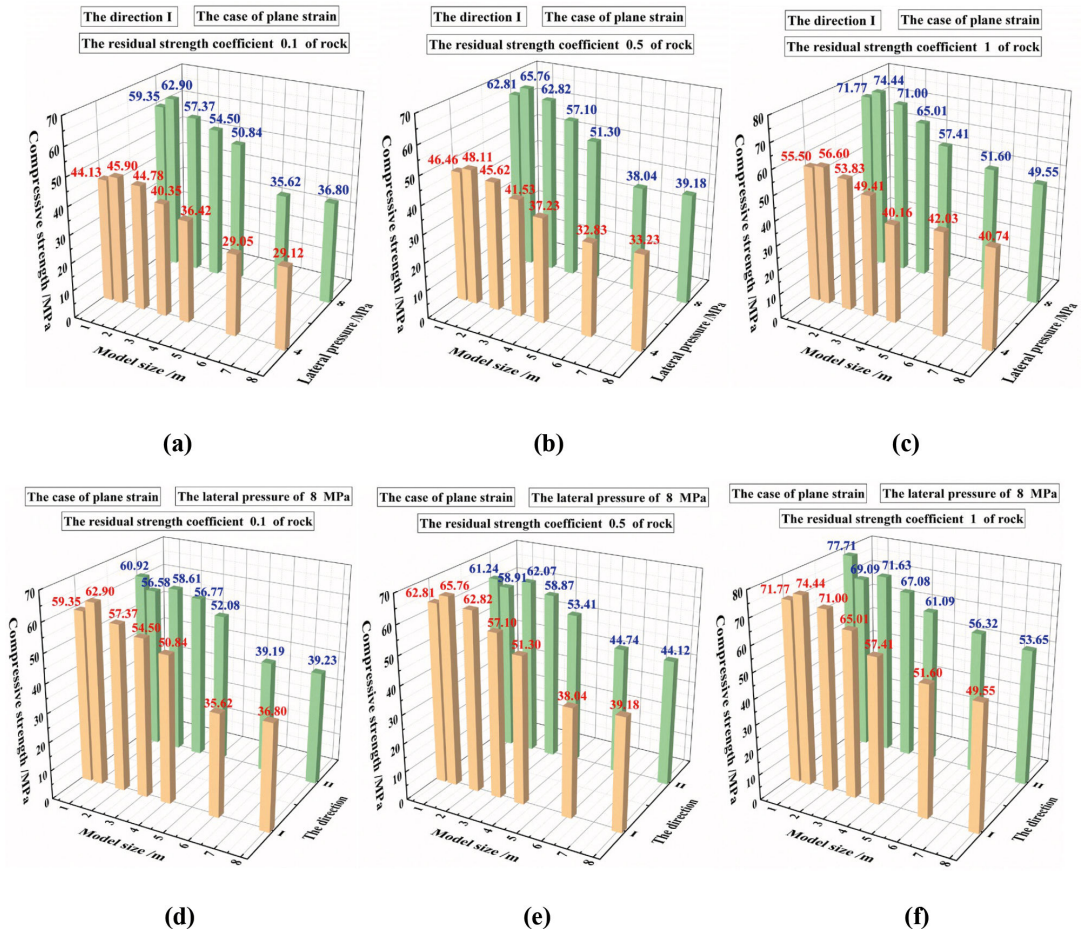

Figure 6: Compressive strengths of the CJBs with different rock meso-constitutive relations and model sizes under the plane strain case: (a)–(c) direction I when the lateral pressures = 4 and 8 MPa; (d)–(f) directions I and II when the lateral pressure = 8 MPa.

and the whole variation range is relatively small for the case between plane stress and plane strain. Furthermore, the ratio of the maximum CS to the minimum CS is 1.076. By contrast, the CS of CJBs decreases at first and then varies moderately, and the whole variation range is relatively large for the plane strain case. At the same time, the ratio of the maximum CS to the minimum CS is 1.729. In Figure 8(b), it can be seen that the variation trend of CS with the growth of the model size is similar along directions I and II perpendicular to the column axis. At the same time, for the plane strain case, the ratio of the maximum value to the minimum value of CSs is 1.407. Additionally, as can be seen in Figures 8(a) and 8(b), the CSs of CJBs for the plane strain case are relatively high in comparison with the case between plane stress and plane strain. When the model size is 0.5–4 m, the CS difference between the two kinds of model boundaries is especially obvious.

As can be seen in Figure 8(c), for direction I, the EDM of CJBs shows the trend of first growth, slow change, second growth, and then gentle variation for the case between plane stress and plane strain. Furthermore, the ratio of the maximum EDM to the minimum EDM is 1.141. For the plane strain case, the EDM of CJBs displays a fluctuating trend, and the ratio of the maximum EDM to the minimum EDM is 1.107. As is displayed in Figure 8(d), the EDM of CJBs fluctuates as the model size rises in direction II perpendicular to the column axis and the two boundary conditions. The ratio of the maximum value to the minimum value of EDMs is 1.035 for the case between plane stress and plane strain. Furthermore, the ratio of the maximum value to the minimum value of EDMs is 1.056 for the plane strain case. Moreover, as depicted in Figures 8(c) and 8(d), the EDMs of CJBs for the plane strain case are larger than in the case between plane stress and plane strain.

3.2. The Multistage Mechanical and Damage Behavior and Energy Evolution of the CJBs

3.2.1. The Plane Strain Case

3.2.1.1. Meso-Constitutive Relation. In Figure 9, stages I, II, and III are the stress growth stage, the stress drop stage, and the residual strength stage, respectively. Figure 10 presents the various mechanical stages of the CJBs with different rock meso-constitutive relations (i.e., the

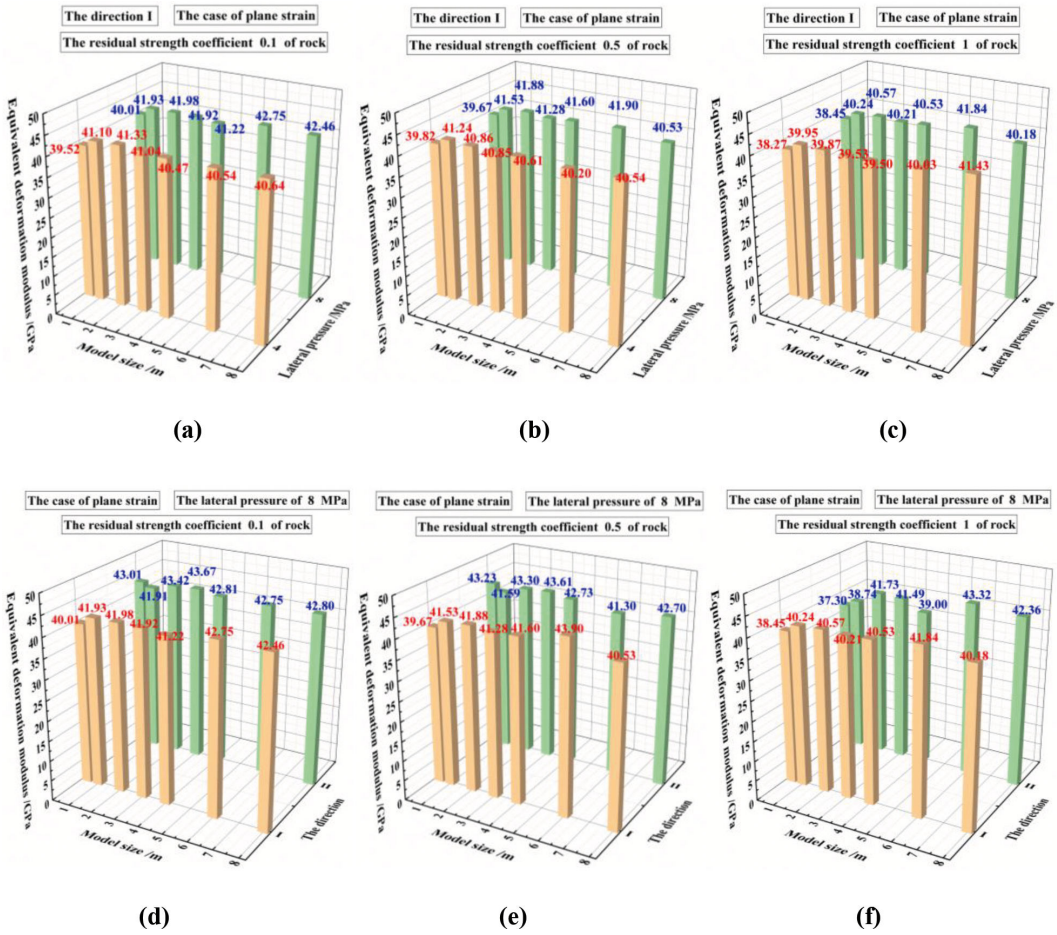

FIGURE 7: Equivalent deformation moduli of the CJBs with different rock meso-constitutive relations and model sizes under the plane strain case: (a)–(c) direction I when the lateral pressures = 4 and 8 MPa; (d)–(f) directions I and II when the lateral pressure = 8 MPa.

RSCs = 0.1, 0.5, and 1.0) and model sizes of 4 and 8 m. As can be seen in Figures 10(a) and 10(b), for the CJBs with a model size of 4 m and an RSC of 0.1 along direction I when the lateral pressure = 4 and 8 MPa, stages I and II are obvious; when the RSC is 0.5 or 1.0, stages I, II, and III are all obvious on the stress–strain curves. As can be seen in Figures 10(c) and 10(d), for the CJBs with a model size of 4 m and RSCs of 0.1, 0.5, and 1.0 along direction II when the lateral pressure = 4 MPa, stages I, II, and III are reproduced on the stress–strain curves. When the lateral pressure = 8 MPa and the RSC of rock is 0.1 or 1.0, stages I and II are obvious on the stress–strain curves; when the RSC of rock is 0.5, stage I, stage II, and a short stage III can be observed before the final failure.

As can be seen in Figures 10(e) and 10(f), for the CJBs with a model size of 8 m and an RSC of 0.1 along direction II when the lateral pressure = 4 MPa, there are only stages I and II on the stress–strain curve; when the RSC is 0.5 or 1.0, there are stage I, stage II, and a short stage III on the stress–strain curves. When the lateral pressure is set to 8 MPa, and the RSC is 0.1 or 0.5, there are only stages I and II on the stress–strain curves; when the RSC is 1.0, there are stages I, II, and III on the stress–strain curve.

Figure 11 displays the multistage damage behaviors of the CJBs with a model size of 4 m and RSCs of 0.1, 0.5, and 1.0 along directions I and II perpendicular to the column axis when the lateral pressure = 8 MPa under plane strain. When the rock RSC = 0.1 along direction I, during stage I, the vertical joints inside the specimen are damaged; during stage II, the columns at the upper part of the sample are damaged and broken. When the rock RSC = 0.5, during stages II and III, an M-type damaged area gradually occurs at the upper part of the specimen. When the rock RSC = 1.0, during stages II and III, the damaged areas at the upper part of the sample show strip characteristics.

As can be seen in Figure 11, for direction II, when the RSC is 0.1, during stage I, the oblique joints inside the specimen are damaged, and some vertical joints near the top of the specimen are damaged and broken to a certain extent; during stage II, a V-shaped damaged zone forms at the upper middle part of the sample. Furthermore, damaged areas also appear at both the upper left and upper right parts of the sample. When the rock RSC = 0.5, the damage evolution of the specimen is similar to

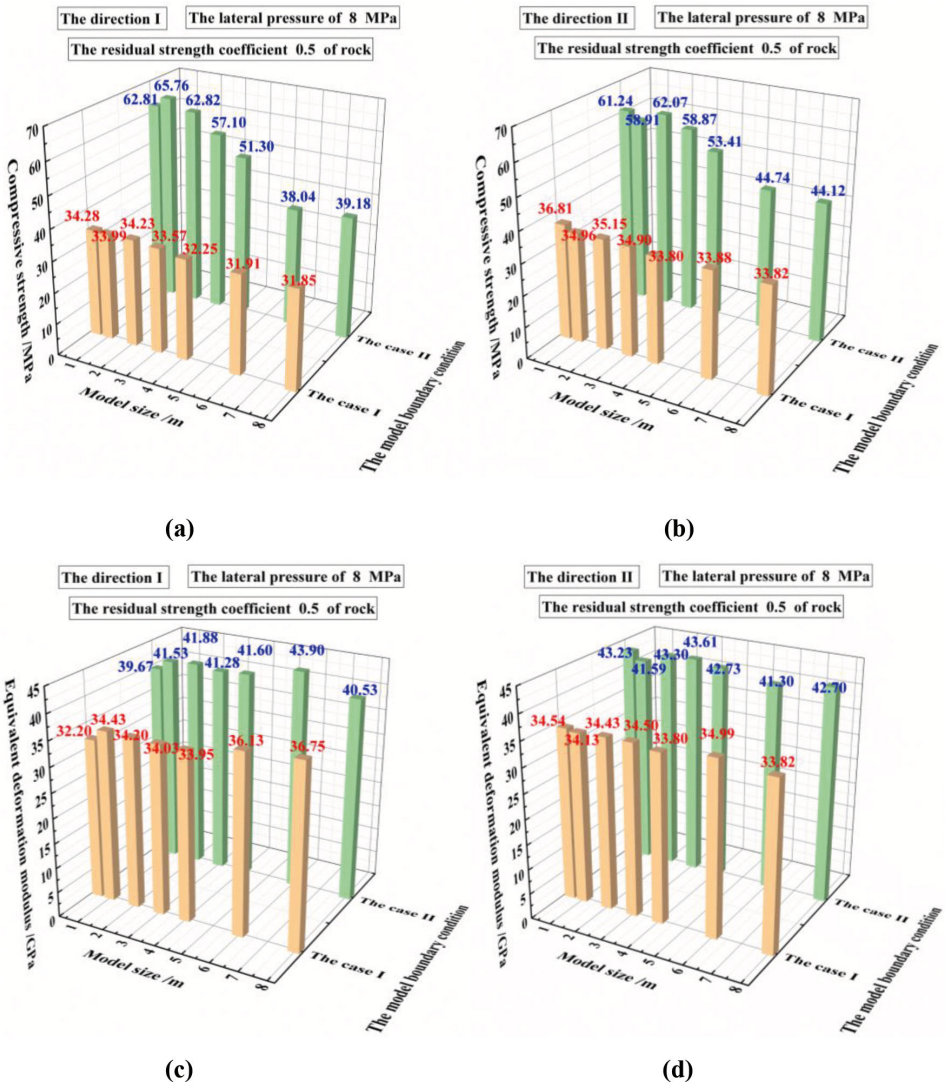

Figure 8: For the CJBs with different boundary conditions and model sizes: (a) and (b) the CSs of the CJBs along directions I and II; (c) and (d) the EDMs of the CJBs along directions I and II.

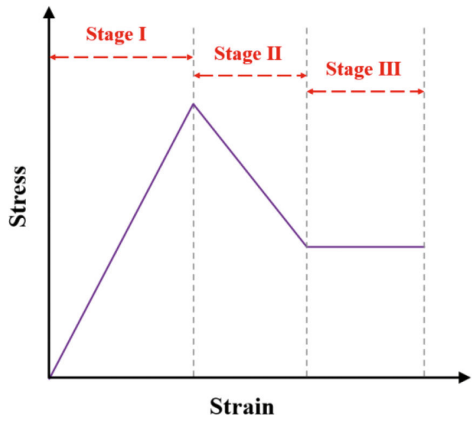

Figure 9: Different stages of the stress–strain curve of CJBs.

that of the specimen with a rock RSC of 0.1. However, the damage evolution of the former continues to stage III, while the damage evolution of the latter only develops to stage II. When the rock RSC = 1.0, during stage I, damage develops at the oblique joints and the vertical joints within the upper part of the sample are damaged and broken; during stage II, there are several strip zones damaged and fractured at the upper part of the sample, one of which propagates to the middle left part of the specimen.

In Figure 12, it can be seen that along direction I, when the RSC is 0.1, during stage I, the vertical joints at the upper part of the sample are damaged, and the columns at the upper middle part of the sample begin to show damage; during stage II, the damaged and crushed range at the upper middle part of the sample further develops, and a damaged zone also appears at the upper left and right parts of the sample. When the rock RSC = 0.5, the damage evolution of the specimen is similar, but the damage range of the former is smaller than the latter. When the rock RSC = 1.0, during stage I, the columns are damaged at the upper

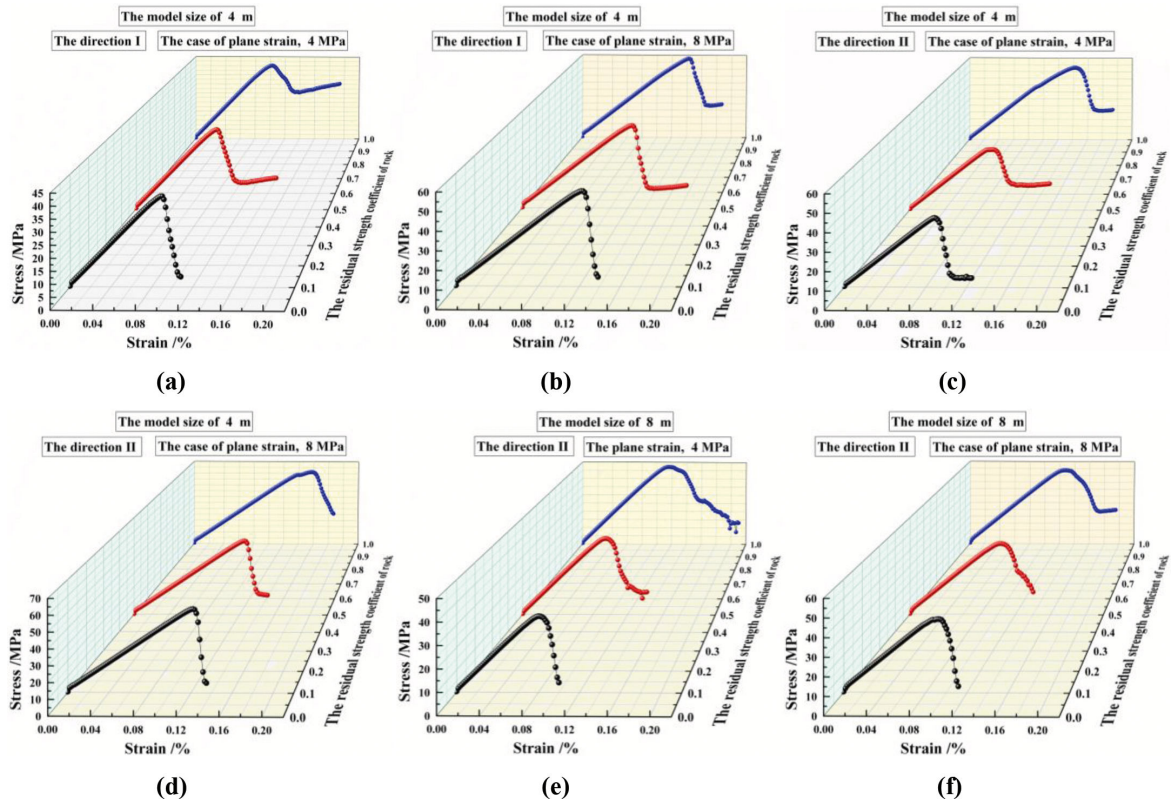

FIGURE 10: The stress–strain relationships of the CJBs under plane strain: (a) and (b) for the CJBs with a model size of 4 m along direction Ⅰ under the lateral pressures of 4 and 8 MPa; (c) and (d) for the CJBs with a model size of 4 m along direction II; (e) and (f) for the CJBs with a model size of 8 m along direction Ⅱ.

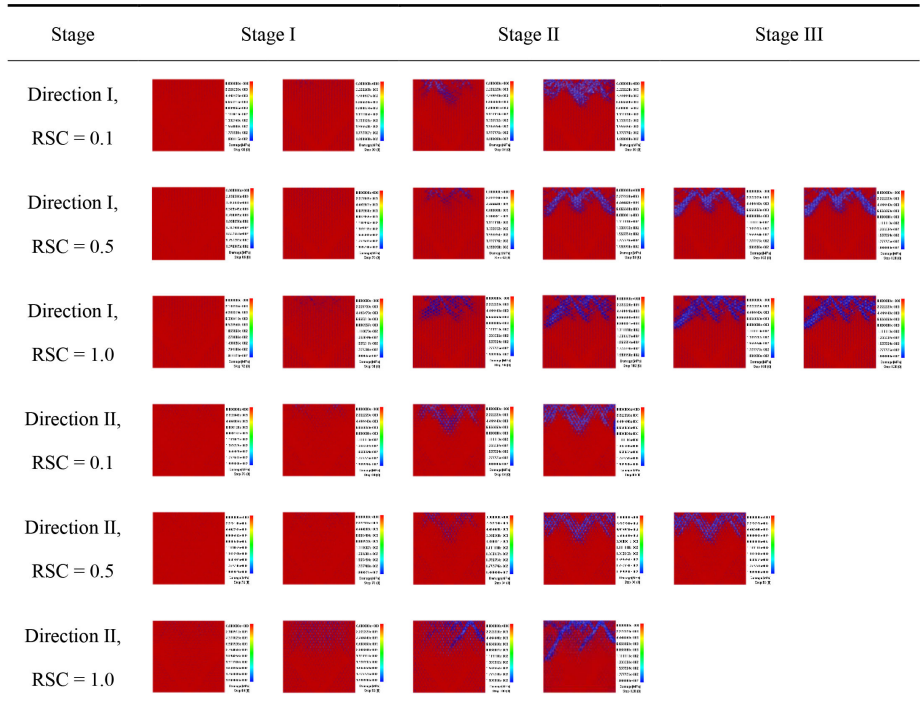

FIGURE 11: The multistage damage behaviors of the CJBs with a model size of 4 m and different rock meso-constitutive relations along directions I and II when the lateral pressure = 8 MPa under plane strain.

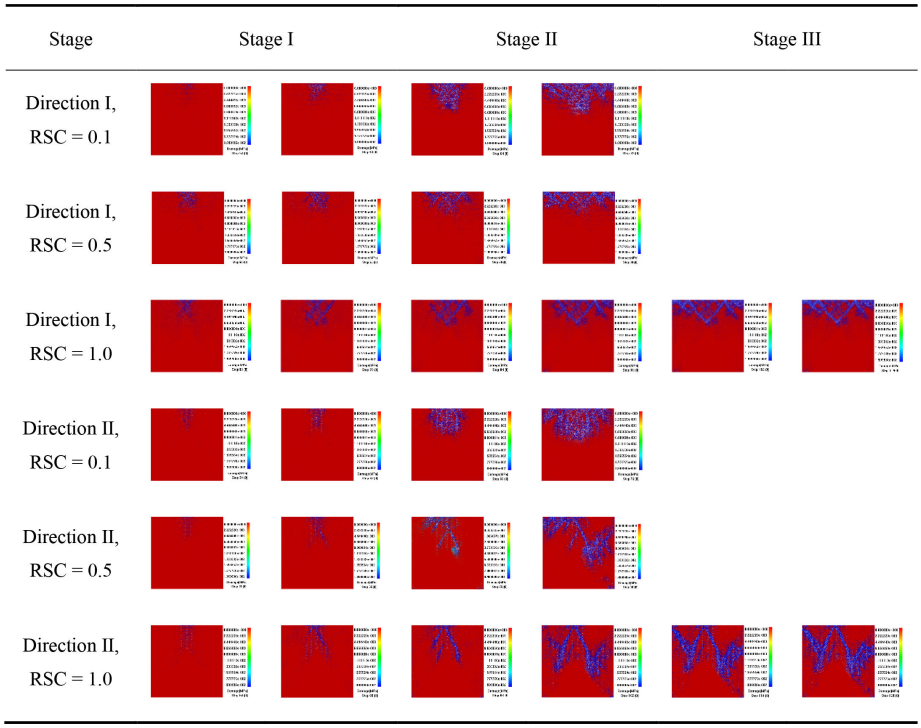

Figure 12: The multistage damage behaviors of the CJBs with a model size of 8 m and different rock meso-constitutive relations along directions I and II when the lateral pressure = 8 MPa under plane strain.

middle part of the sample, and strip-shaped damaged areas are developed; during stage II, the damage zone at the upper part of the specimen grows, reaching the upper right part of the sample; during stage III, the damaged areas appear at the upper left part of the sample, and the breakage of the damaged zone intensifies.

As is depicted in Figure 12, when the rock RSC = 0.1 along direction II, the damage evolution of the specimen is similar to that of the specimen with a rock RSC of 0.1 along direction I. When the rock RSC = 0.5, during stage II, several strip-shaped damaged zones gradually form inside the specimen. Additionally, obvious damaged areas appear in the middle right part of the specimen. When the rock RSC = 1.0, during stage I, damaged areas gradually develop at the upper middle part of the specimen; during stage II, an inverted V-shaped damage zone gradually forms inside the specimen; and during stage III, the damaged zones occur at the upper left and middle right parts of the specimen.

Figure 13 shows the energy evolutions of the CJBs with different RSCs of 0.1, 0.5, and 1.0 and model sizes of 4 and 8 m. As can be seen in Figure 13(a), for a model size of 4 m and a lateral pressure of 4 MPa along direction I, with an increase in the rock RSC, the peak value of AE energy drops gradually. Furthermore, when the rock RSC is 0.1, the AE energy basically presents a single-peak shape distribution; when the rock RSC is 0.5, the AE energy shows a trend of inapparent double-peak shape distribution; and when the rock RSC is 1.0, the AE energy shows a double-peak shape distribution to a certain extent. Furthermore, when the rock RSC is 0.1 or 0.5, the peak values of AE energies appear roughly in the same order on the strain axis; when the rock RSC is 1, the peak AE energy value lags behind the former on the strain axis. As can be seen in Figure 13(b), for a model size of 4 m and a lateral pressure of 8 MPa along direction I, when the rock RSC is 0.1 or 1.0, the peak values of AE energy are almost equal; when the rock RSC is 0.5, the peak AE energy value is relatively small. At the same time, when the rock RSC is 0.1, 0.5, or 1.0, the AE energy presents a single-peak shape distribution. When the rock RSC is 0.1 or 0.5, the peak values of AE energy appear roughly in the same order on the strain axis; when the rock RSC is 1, the peak AE energy value lags slightly on the strain axis.

As can be seen in Figure 13(c), with a model size of 4 m and a lateral pressure of 4 MPa along direction II, as the rock RSC increases, the peak value of AE energy decreases first and then increases. When the rock RSC is 0.1, 0.5, or 1.0, the AE energy shows a double-peak shape distribution, and with an increase in the rock RSC, the spacing between the two peaks broadens. When the rock RSC is 0.1 or 0.5, the order difference between the AE energy peaks on the strain axis is relatively small; when the rock RSC is 1.0, the peak AE energy value lags obviously on the strain axis. In Figure 13(d), it can be seen that with a model size of 4 m and a lateral pressure of 8 MPa along direction II, when the rock RSC is 0.1 or 0.5, the difference in the peak values of AE energy is very small; when the rock RSC is 1.0, the peak AE energy value is low. Moreover, when the rock RSC is 0.1 or 0.5, the AE energy has a single-peak shape distribution; when the rock RSC is 1.0, the AE energy displays a double-peak shape distribution. Moreover, the

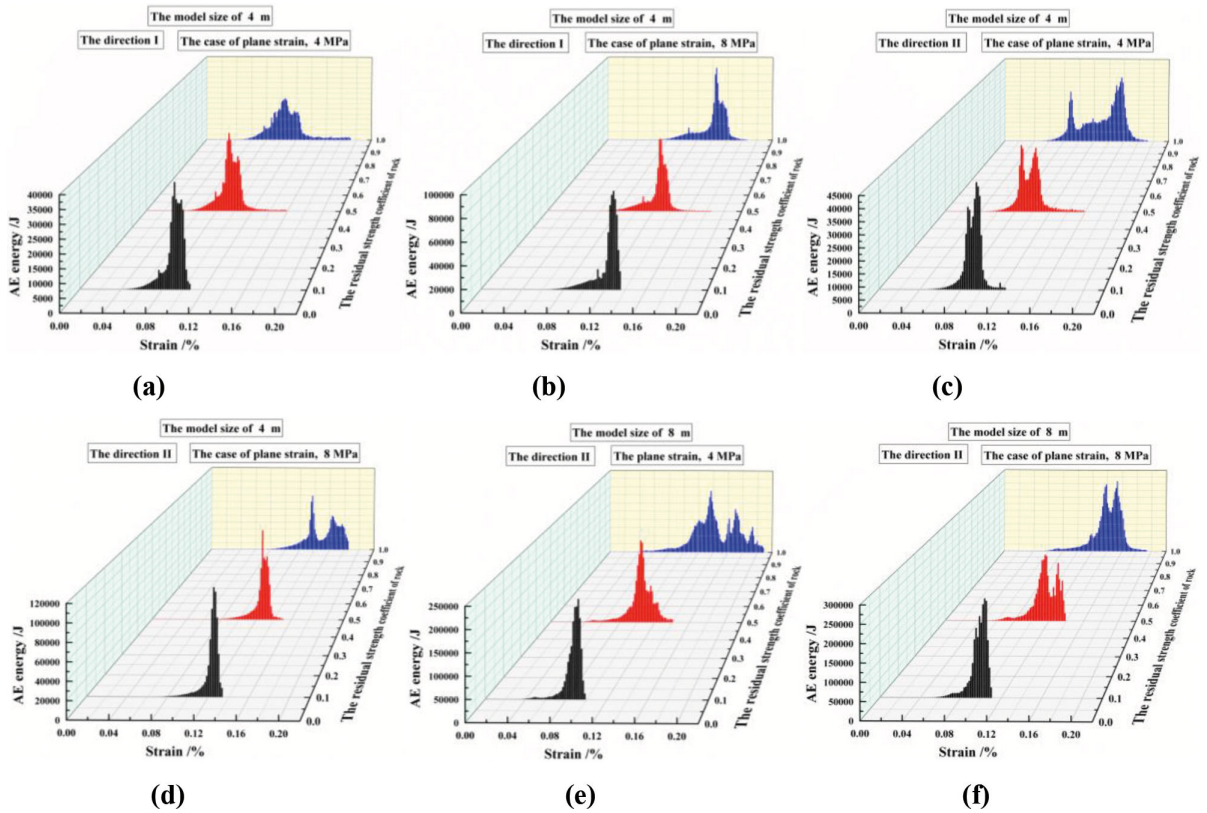

FIGURE 13: Energy evolutions of the CJBs with different rock meso-constitutive relations under plane strain: (a) and (b) CJBs with a model size of 4 m along direction I under the lateral pressures of 4 and 8 MPa; (c) and (d) CJBs with a model size of 4 m along direction II; (e) and (f) CJBs with a model size of 8 m along direction II.

orders between AE energy peaks on the strain axis are relatively close; when the rock RSC is 1.0, the peak AE energy value is behind the former on the strain axis.

In Figure 13(e), we can see that for a model size of 8 m and a lateral pressure of 4 MPa along direction II, with a growth in rock RSC, the peak value of AE energy decreases. Furthermore, when the rock RSC is 0.1 or 0.5, the AE energy has a single-peak shape distribution; when the rock RSC is 1.0, the AE energy shows a multipeak shape distribution. Furthermore, with a rise in rock RSC, the peak AE energy value gradually lags on the strain axis. As can be seen in Figure 13(f), for a model size of 8 m and a lateral pressure of 8 MPa along direction II, as the rock RSC increases, the peak value of AE energy decreases first and then grows. When the rock RSC is 0.1, the AE energy displays a single-peak shape distribution; when the rock RSC is 0.5 or 1, the AE energy presents a rough triple-peak shape distribution with one small peak and two large peaks. This is mainly because the stress concentrations inside the specimens tend follow a banded distribution with increasing load, resulting in the gradual development of the banded damage-fracture zones. At the same time, with a growth in rock RSC, the peak AE energy value also progressively lags on the strain axis.

3.2.1.2 Model Size. As can be seen in Figure 14(a), for a model size of 0.5–8 m and a lateral pressure of 4 MPa along direction I, stages I, II, and III can be observed on the stress–strain curves. As can be seen in Figure 14(b), for a model size of 0.5–6 m and a lateral pressure of 8 MPa, there are stages I, II, and III on the stress–strain curves; if the model size = 8 m, there are only stages I and II on the stress–strain curve. As is shown in Figure 14(c), for a model size of 0.5–4 m and a lateral pressure of 4 MPa along direction II, there are stages I, II, and III on the stress–strain curves; if the model size increases to 6 m, there are only stages I and II on the stress–strain curve; when the model size is 8 m, there are stages I, II, and a short stage III on the stress–strain curve. As is shown in Figure 14(d), for a model size of 0.5 and 4 m and a lateral pressure of 8 MPa, there are stage I, stage II, and a short stage III on the stress–strain curves; if the model size increases to 1–3 m, there are stages I, II, and III on the stress–strain curves; if the model size reaches 6 and 8 m, there are only stages I and II on the stress–strain curves.

In Figure 15, it can be seen that for a model size of 0.5 m, during stage I, the damage appears at vertical joints; during stage II, the cracks develop at the columns, and fractures are initiated; and during stage III, the breakage of the columns inside the specimen intensifies. For a model size of 1 m, during stage I, the damage mainly occurs at vertical joints; during stage II, the columns within the upper area of the sample are damaged, and fracture initiations appear. At the same time, damage to the columns occurs at the lower part of the specimen; during stage III, the breakage of the columns within the upper area of the sample is

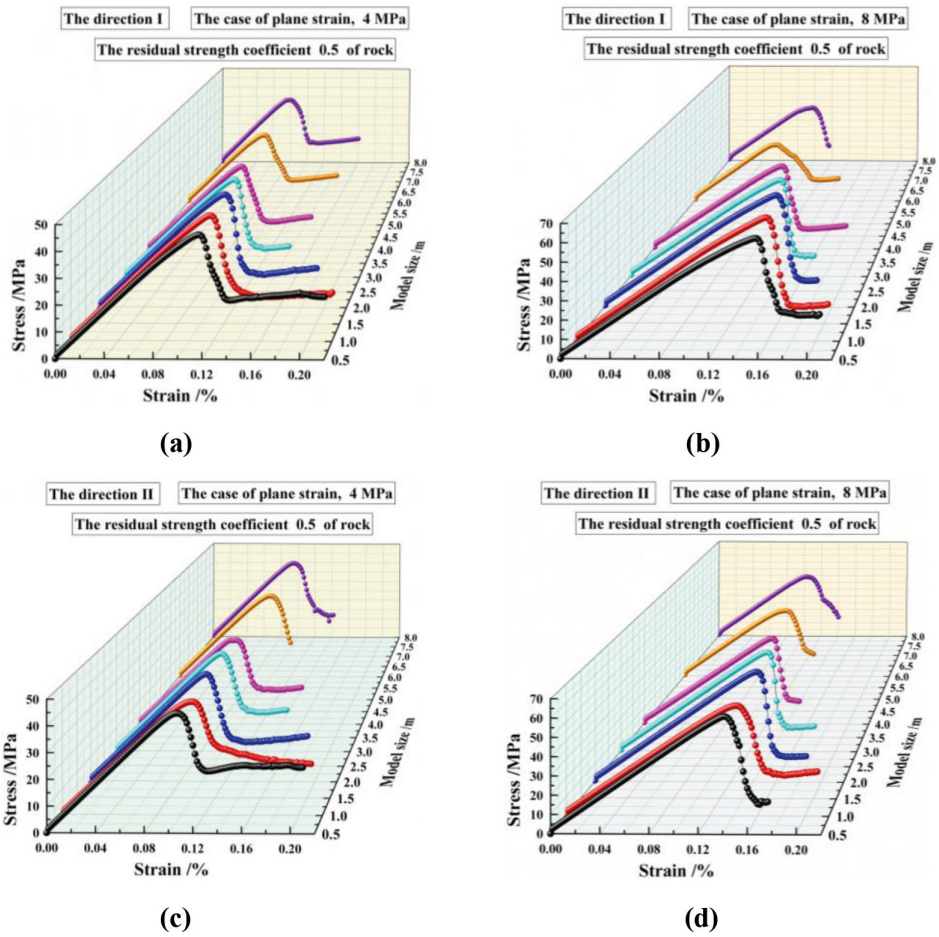

Figure 14: The multistage mechanical behaviors of the stress–strain curves of the CJBs with different model sizes under plane strain.

aggravated. For a model size of 2 m, during stage II, several columns within the upper and lower areas of the sample are damaged, and then fractures initiate, connect, and form strip-damaged zones; during stage III, the breakage of the damaged zones is intensified. For the model sizes of 3 and 4 m, during stage II, an M-shaped damaged area gradually forms at the upper part of the specimen; during stage III, the crushing of the M-shaped damage zone is aggravated. For model sizes of 6 and 8 m, during stage I, the damage to the columns at the upper middle part of the sample develops and cracks initiate; during stage II (and stage III), the range of damage and number of fractures increase. Clearly, they also occur at the upper left and right parts of the sample.

Figure 16 shows the energy evolutions of the CJBs with different model sizes when the rock RSC = 0.5 and the lateral pressure is 4 and 8 MPa along directions I and II perpendicular to the column axis under plane strain. As can be seen in Figure 16(a), for CJBs with a lateral pressure of 4 MPa along direction I, the peak AE energy value increases with a growth in model size. When the model size is 6 m, the AE energy presents a double-peak shape distribution; when the model is of other sizes, the AE energy has a single-peak shape distribution. In terms of the order in which the peak AE energy values appear on the strain axis, the larger the model size, the farther forward the peak value of AE energy occurs on the strain axis. As can be seen in Figure 16(b), for the CJBs with a lateral pressure of 8 MPa along direction I, the peak value of AE energy first grows, then decreases, and then increases with an increase in the model size. Furthermore, if the model size equals 6 m, the AE energy roughly displays a triple-peak distribution; if the model size increases to 8 m, the AE energy presents a double-peak distribution; when the model is of other sizes, the AE energy shows a single-peak distribution.

As can be seen in Figure 16(c), for the CJBs with a lateral pressure of 4 MPa along direction II, the peak value of AE energy grows as the model size increases. When the model size is 4 m, the AE energy shows a double-peak distribution; when the model is of other sizes, the AE energy displays a single-peak distribution. In terms of the order in which the peak AE energy values appear on the strain axis, with an increase in the model size, the peak AE energy value first moves forward on the strain axis, then lags, and then moves forward. As can be seen in Figure 16(d), for the CJBs with a lateral pressure of 8 MPa along direction II, the peak value of AE energy rises as the model size increases. When the model size is 8 m, the AE energy

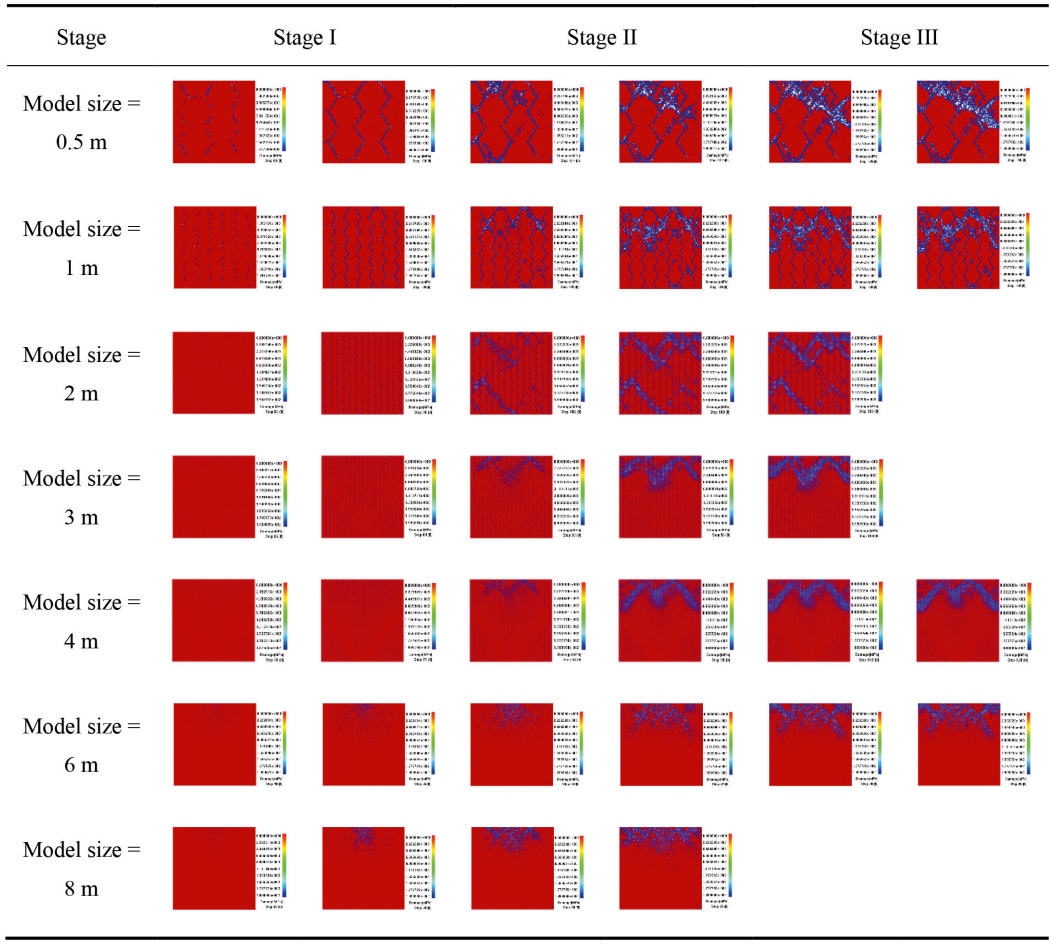

FIGURE 15: The multistage damage behaviors of the CJBs with different model sizes when the RSC = 0.5 and the lateral pressure = 8 MPa along the direction I under plane strain.

presents a multipeak distribution; when the model is of other sizes, the AE energy shows a single-peak distribution.

3.2.2. The Case between Plane Stress and Plane Strain. Figure 17 shows the multistage mechanical behaviors of the CJBs when the rock RSC = 0.5 and the lateral pressure = 8 MPa along directions I and II perpendicular to the column axis. In Figure 17(a), we can see that when the model size is 0.5–2 m along direction I, there are only stages I and II on the stress–strain curves; if the model size is 3–8 m, there are stages I, II, and III on the stress–strain curves. Figure 17(b) indicates that for the model sizes of 0.5–4 m along direction II, there are only stages I and II on the stress–strain curves; if the model size increases to 6–8 m, there are stages I, II, and III on the stress–strain curves.

In Figure 18, it can be seen that for the model sizes of 0.5–2 m, during stage I, the horizontal joints inside the specimen are damaged; and during stage II, several vertical joints inside the sample become broken. If the model size = 3 m, during stages II and III, the columns at the upper middle part of the sample fail. For a model size of 4 m, during stage II, the strip-damaged zones form inside the specimen. For the model sizes of 6 and 8 m, during stages II and III, the columns at the upper part of the sample become damaged and broken.

As can be seen in Figures 19(a) and 19(b), at a lateral pressure of 8 MPa along directions I and II, the peak value of AE energy grows with an increase in the model size. Furthermore, the AE energy displays a single-peak shape distribution, and the peak AE energy value moves forward on the strain axis slowly, although it is not obvious.

3.3. The AE Energy Characteristics of the CJBs with Different Rock Meso-Constitutive Relations and Model Sizes under Lateral Pressure

3.3.1. The Plane Strain Case

3.3.1.1. Meso-Constitutive Relation. Figure 20 presents the AE energy accumulations of the CJBs with different rock meso-constitutive relations (i.e., the RSC equals 0.1, 0.5, and 1, respectively) and model sizes of 4 and 8 m along directions I and II perpendicular to the column axis when the lateral pressure equals 4 or 8 MPa. In Figures 20(a)

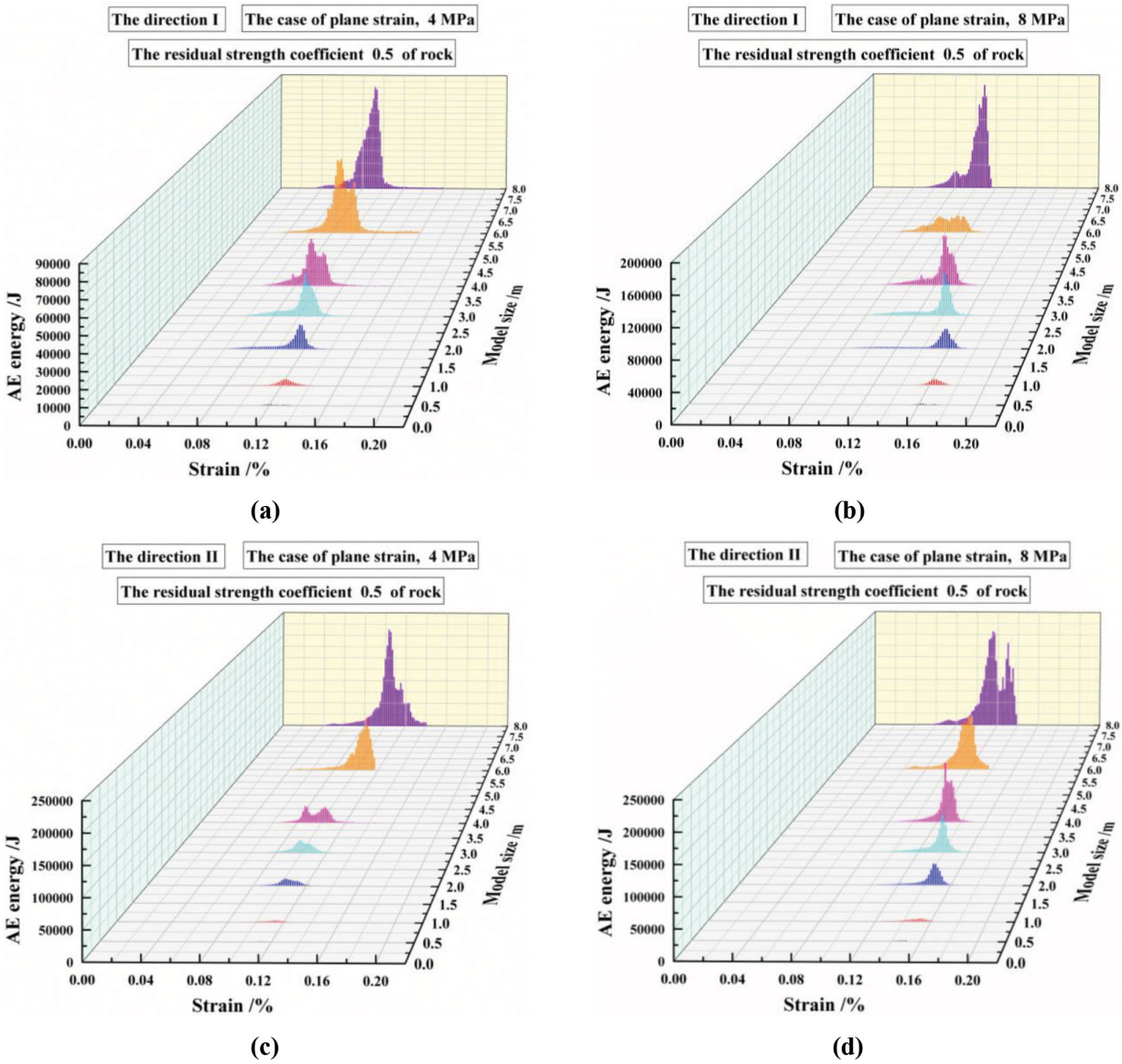

Figure 16: The energy evolutions of the CJBs with different model sizes under plane strain.

and 20(b), when the model size is 4 m, the rock RSC is 0.1, and the pressure is 4 or 8 MPa along direction I, the AE energy accumulates slowly in the beginning and very quickly after that; and when the rock RSC is 0.5 or 1, the AE energy accumulates slowly in the beginning. Later, this process becomes quick but then slows down again.

As can be seen in Figures 20(c) and 20(d), when the model size is 4 m, the rock RSC is 0.1–1, and the lateral pressure is 4 MPa along direction II, the AE energy accumulates slowly in the beginning. Later, it rises more quickly but then varies slightly. When the rock RSC is 0.1 or 1 and the lateral pressure is 8 MPa, the accumulation of AE energy changes slightly in the beginning and then grows; when the rock RSC is 0.5, the accumulation of AE energy varies slightly in the beginning, then increases quickly, and after that varies slightly.

As can be seen in Figures 20(e) and 20(f), when the model size is 8 m, the rock RSC is 0.1 or 1 and the lateral pressure is 4 MPa along direction II, the AE energy accumulates slowly in the beginning but speeds up; when the rock RSC is 0.5, the AE energy accumulates slowly at first, then quickly, and then slowly again. When the lateral pressure is 8 MPa and the rock RSC is 0.1 or 0.5, the AE energy accumulates slowly in the beginning and then quickly; when the rock RSC is 1, the AE energy accumulates slowly in the beginning, then quickly, and after that slowly again.

Figure 21 shows the strains and AE energy accumulations corresponding to the peak stresses of the CJBs with various rock meso-constitutive relations (i.e., the RSC is 0.1, 0.5, or 1) and model sizes of 4 and 8 m along directions I and II perpendicular to the column axis. As can be seen in Figure 21(a), when the model size is 4 m and the lateral pressure is 4 or 8 MPa along direction I, with the growth

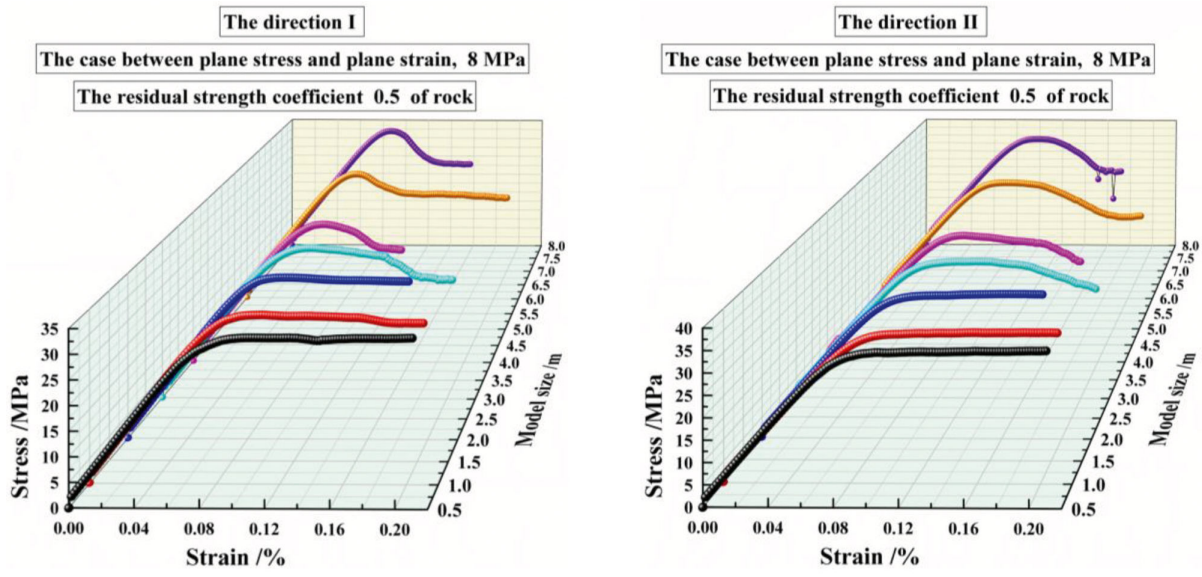

Figure 17: Different stages of stress–strain curves of the CJBs with different model sizes under the case between plane stress and plane strain.

in the rock RSC, the strain and AE energy accumulation corresponding to the peak stress are slow at first and then increase. Additionally, with a rise in the lateral pressure, the strain and AE energy accumulation corresponding to the peak stress grow gradually. As can be seen in Figure 21(b), when the model size is 4 m and the lateral pressure is 4 or 8 MPa along direction II, the strain and AE energy accumulation corresponding to the peak stress grow slowly and then quickly as the rock RSC increases. Moreover, as the lateral pressure increases, the strain and AE energy accumulation corresponding to the peak stress rise.

As is displayed in Figure 21(c), when the model size is 8 m and the lateral pressure is 4 or 8 MPa along direction I, the strain corresponding to the peak stress increases with a growth in rock RSC. Furthermore, when the lateral pressure is 4 MPa, with a rise in rock RSC, the AE energy accumulation corresponding to peak stress varies slightly at first and then grows; if the lateral pressure increases to 8 MPa, the related AE energy accumulation corresponding to peak stress increases. As is shown in Figure 21(d), with a model size of 8 m and a lateral pressure of 4 or 8 MPa along direction II, the strain corresponding to the peak stress rises gradually as the rock RSC increases. Furthermore, if the lateral pressure equals 4 MPa, the AE energy accumulation corresponding to peak stress increases with the growth in rock RSC; if the lateral pressure rises to 8 MPa, the related AE energy accumulation, which corresponds to peak stress, shows an increasing trend.

3.3.1.2. Model Size. In Figure 22(a), we can see that when the model size is 0.5–8 m and the lateral pressure is 4 MPa along direction I, the AE energy accumulates slowly in the beginning, then quickly, and after that slowly as the load continues to increase. As is shown in Figure 22(b), when the model size is 0.5–6 m and the lateral pressure is 8 MPa, the AE energy accumulates with a low ratio initially. Later, it rises quickly and then varies slightly. If the model size equals 8 m, the AE energy accumulation shows a trend of varying slowly and then rising quickly. In addition, with an increase in model size, the growth stage of AE energy accumulation moves forward on the strain axis. As can be seen in Figures 22(c) and 22(d), when the model size is 0.5–4 m and the lateral pressure is 4 or 8 MPa along direction II, the AE energy accumulation changes slowly initially, then grows quickly, and after that varies slowly as the load continues; when the model size is 6 or 8 m, the accumulated AE energy displays a trend of changing slowly and then increasing quickly. Moreover, with an increase in the model size, the growth stage of AE energy accumulation also moves forward on the strain axis.

According to Figure 23(a), when the lateral pressure is 4 or 8 MPa along direction I, with a growth of the model size, the strain corresponding to the peak stress decreases first and then varies slightly (or increases slightly), while the AE energy accumulation corresponding to the peak stress rises gradually. Additionally, as the lateral pressure grows, the energy accumulation of the AE, which corresponds to peak stress, increases, and the extent to which it increases rises as the model size increases. As is shown in Figure 23(b), when the lateral pressure is 4 or 8 MPa along direction II, with an increase in the model size, the strain corresponding to the peak stress changes slightly (or increases slightly), then decreases, and then varies slightly, while the AE energy accumulation corresponding to peak stress grows

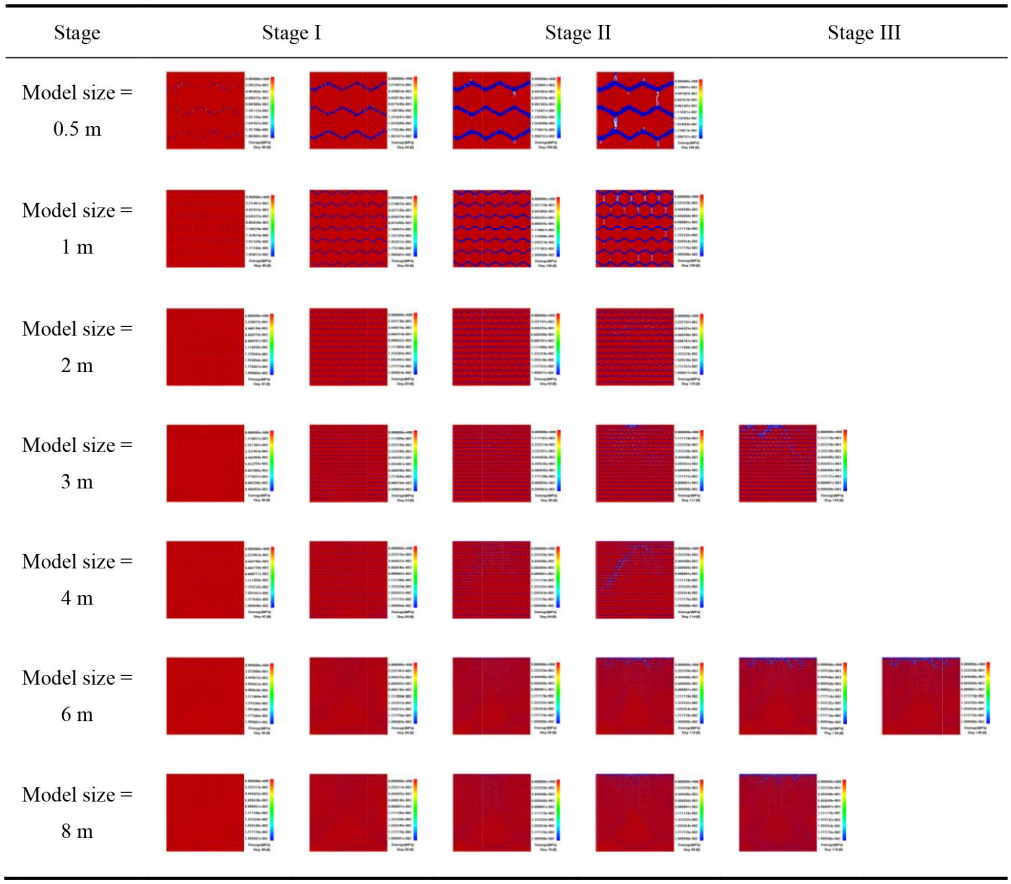

Figure 18: The multistage damage of the CJBs with a rock RSC of 0.5 and lateral pressure of 8 MPa along the direction II under the case between plane stress and plane strain.

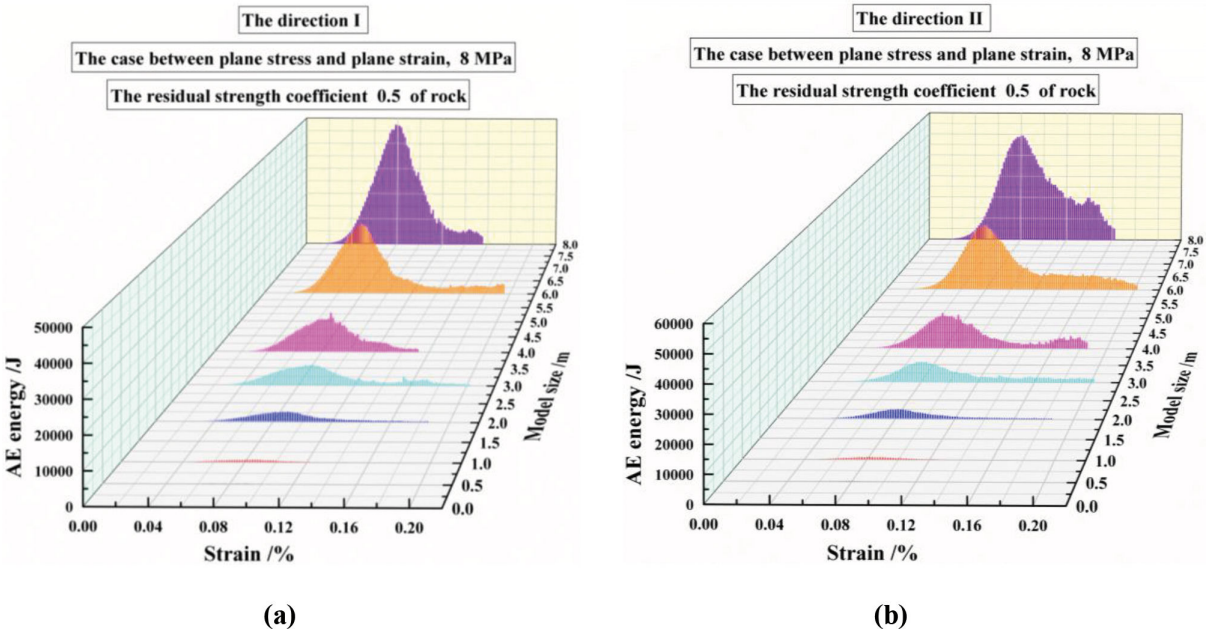

Figure 19: The energy evolution of CJBs with different model sizes under the case between plane stress and plane strain.

gradually. Moreover, as the lateral pressure rises, the strain corresponding to peak stress increases, but the extent to which it increases decreases with the growth of the model size. As the lateral pressure increases, the

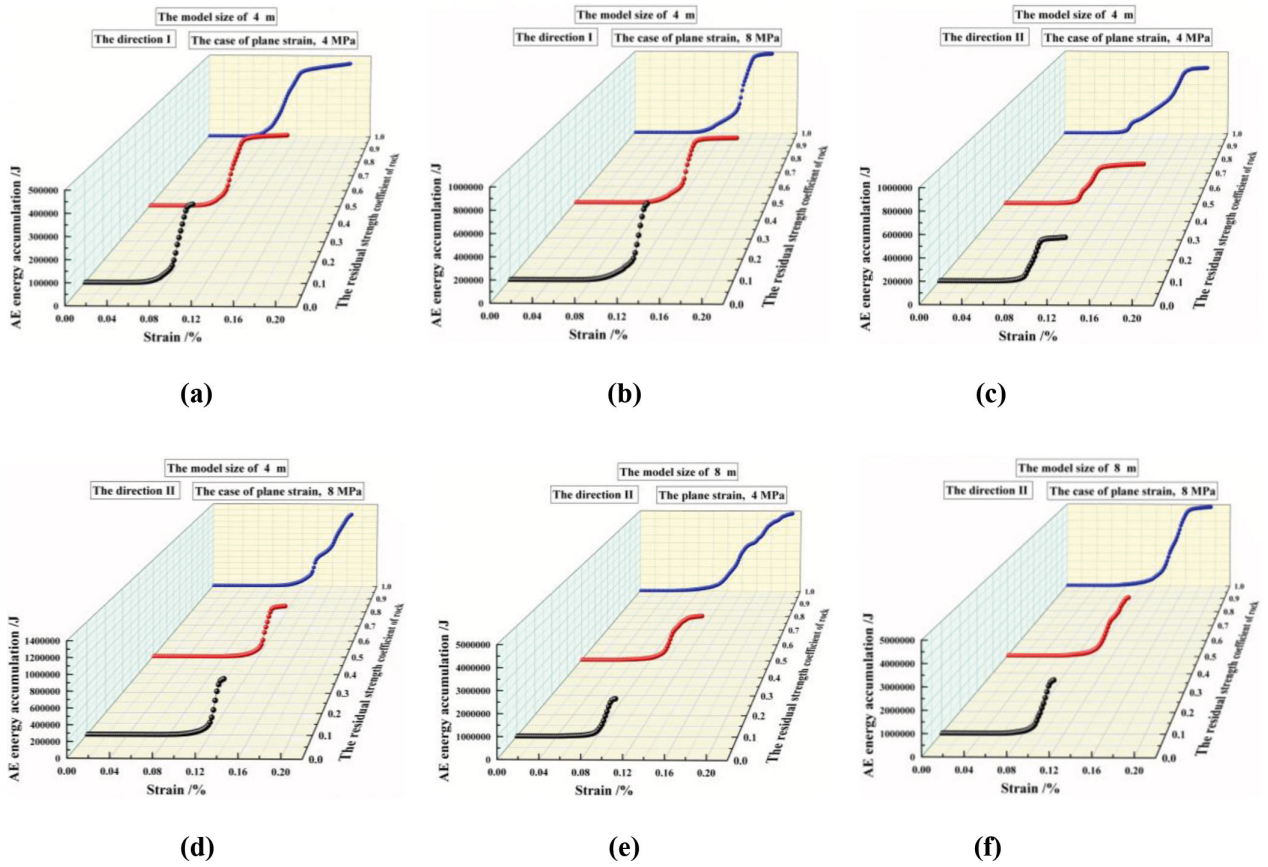

FIGURE 20: AE energy accumulations of the CJBs with different rock meso-constitutive relations under plane strain: (a) and (b) for a model size of 4 m with lateral pressures of 4 and 8 MPa along direction I; (c) and (d) for a model size of 4 m along direction II; (e) and (f) for a model size of 8 m along direction II.

energy accumulation of the AEs, which corresponds to the peak stress, rises, but the extent to which it rises grows first and then changes slowly with a growth in the model size.

3.3.2. The Case between Plane Stress and Plane Strain. It can be seen in Figure 24(a) that for the CJBs with the model size 0.5–8 m along direction I, the energy accumulation of AE changes slightly at first, then grows quickly, and then varies slowly as the load continues. According to Figure 24(b), for the CJBs with a model size of 0.5–6 m along direction II, the AE energy accumulation also displays a trend of varying slowly, then rising quickly, and after that changing slightly; when the model size is 8 m, the AE energy accumulation changes slowly and then grows quickly.

As can be seen in Figure 25, when direction I is considered, the strain corresponding to the peak stress drops first, then grows slightly, and then decreases gradually with a growth in the model size. If direction II is considered, the strain that corresponds to the peak stress fluctuates. Additionally, the specific strain corresponding to the peak stress of the CJBs along direction II is higher than that of the CJBs along direction I. At the same time, the gap grows as the model size increases. Furthermore, according to Figure 25, for the CJBs along directions I and II, the AE energy accumulation corresponding to the peak stress rises gradually with a growth in the model size. Furthermore, the energy accumulation of AE corresponding to the peak stress of the CJBs along direction II is larger than that of the CJBs along direction I. At the same time, the gap increases gradually with a growth in the model size.

4. Discussion

4.1. Influence of Rock Meso-Constitutive Relation and Model Size on Rock Mass Strength and Deformation under Lateral Pressure. The influence of rock meso-constitutive relation and model size on rock mass strength and deformation under lateral pressure can be summarized as follows: when the lateral pressure is 8 MPa, the CS of CJBs rises, and the EDM of CJBs decreases or increases slightly as the rock RSC increases. Furthermore, the CS of CJBs roughly decreases at first and then varies slightly as the model size increases, while the EDM of CJBs fluctuates, but the variation is relatively small.

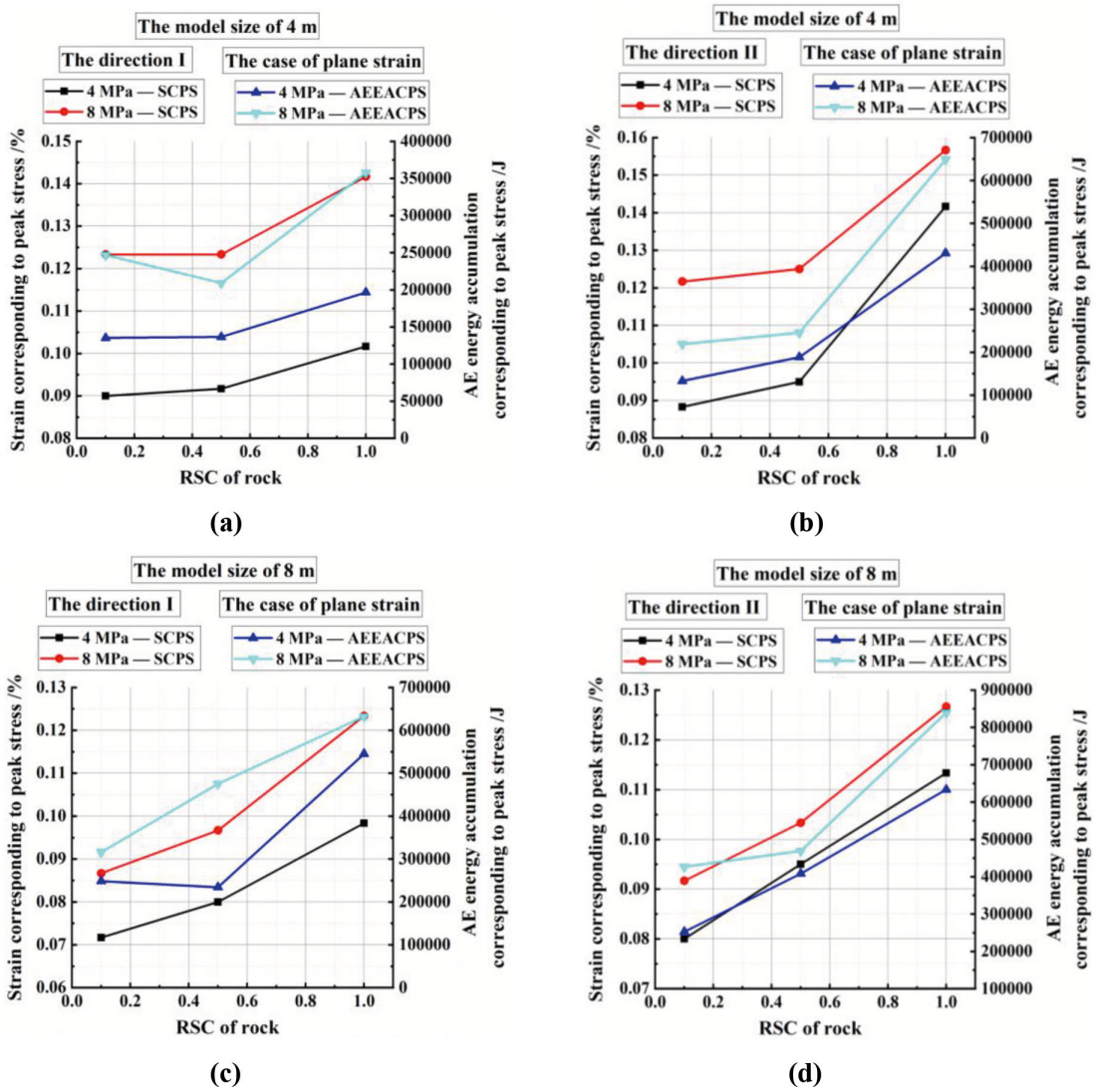

Figure 21: The strains and AE energy accumulations corresponding to the peak stresses of the CJBs with different rock meso-constitutive relations under plane strain.

On the basis of the discrete fracture network (DFN)/discrete element method (DEM), Niazmandi et al. [37] investigated the strength variation of fractured rock masses with different load conditions. Their research showed that the strength of the specimen drops at first and then changes slightly as the sample size increases, which agrees with the results obtained in our study. However, they did not analyze the deformation parameters with different model sizes, and the influence of the meso-constitutive relations on the deformation parameters was not discussed. Fan et al. [38] used a 3D particle flow code (PFC) to investigate the strength and deformability of rocks cut by many nonpersistent joint sets, but the effects of lateral pressure and model size were not considered in their research. Liu et al. [39] adopted the PFC to reveal the anisotropy and scale of the strengths of rocks. Nevertheless, the meso-constitutive relation could vary under lateral pressure in rock engineering, which was not taken into account in their research. Stavrou et al. [40] quantified the influence of size and inhomogeneity on the strengths of rocks with microdefects using the DEM, but the deformation properties were not analyzed further. Wu et al. [41] performed a 3D DEM stress analysis on the scale effect of rock mass mechanical parameters, in which different stress paths were considered. However, different rock meso-constitutive relations under loading stress were not taken into account in their research. Yang et al. [42] investigated the effect of size on the strength and permeability of jointed rock masses using the coupled stress–damage–flow approach. Nevertheless, the deformation property was not discussed, and variations in the rock meso-constitutive model were not considered in their research. Wang et al. [43] discussed the physico-

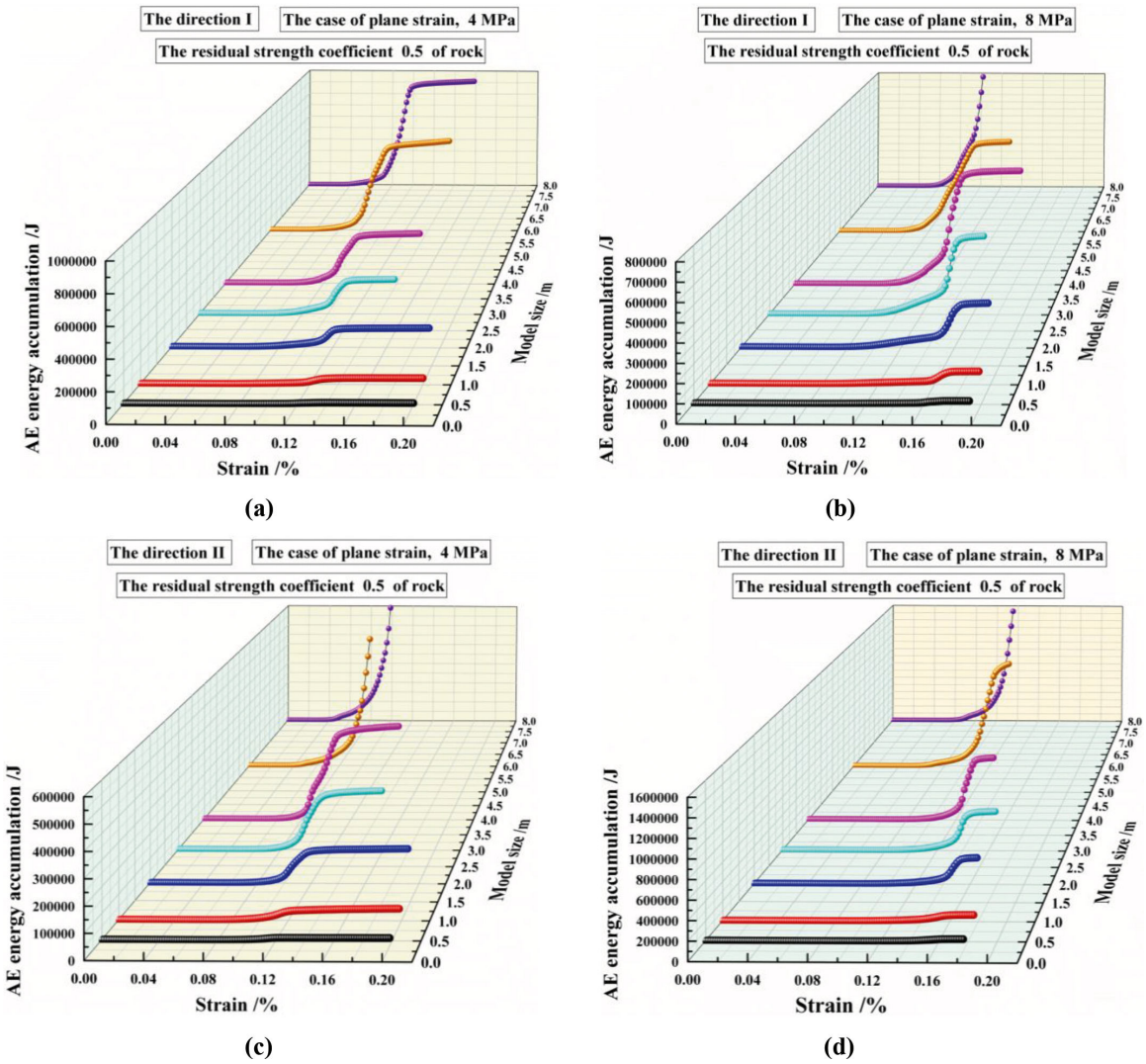

Figure 22: The AE energy accumulations of the CJBs with different model sizes under plane strain.

mechanical parameters of jointed rock masses influenced by transverse joints as well as lateral pressures. However, they did not adopt different rock meso-constitutive relations in their research, which may cause differences in engineering practice.

4.2. Influence of Rock Meso-Constitutive Relation and Model Size on Mechanical Damage of Rock Mass under Lateral Pressure. In terms of the influence of the rock meso-constitutive relation and model size on the mechanical damage of rock masses under lateral pressure, we came to the following conclusions: when the model size is 4 m, the lateral pressure is 8 MPa, and the rock RSC is 0.1 along direction I orthogonal to the column axis, there are obvious stages I and II on the stress–strain curve; when the rock RSC is 0.5 or 1, there are stages I, II, and III on the stress–strain curves. When the model size is 8 m and the rock RSC is 0.1 or 0.5, there are only stages I and II on the stress–strain curves; when the rock RSC is 1, there are stages I, II, and III on the stress–strain relationships. Additionally, the damage behaviors of the CJBs in different stages are investigated.

Using a DFN/DEM approach, Niazmandi et al. [37] obtained stress–strain curves of fractured rock masses under various numerical situations, but the damage evolutions of specimens in different stages of stress–strain curves were not displayed and analyzed, and the influence of rock meso-constitutive relations on them was not investigated. Based on the numerical method of PFC3D, Fan et al. [38] captured the failure processes of jointed rock specimens at different axial strain levels. However, the influence of model size and lateral pressure on the failure process of specimens was not considered in their research. The stress–strain curves and failure modes of defected rock masses were presented by Liu et al. [39] using PFC, but the failure processes of specimens corresponding to different stages of stress–strain curves were not further analyzed. Gao et al. [44] applied a new method to obtain displacement vectors and crack distributions of specimens with bedding plane orientations. Nevertheless,

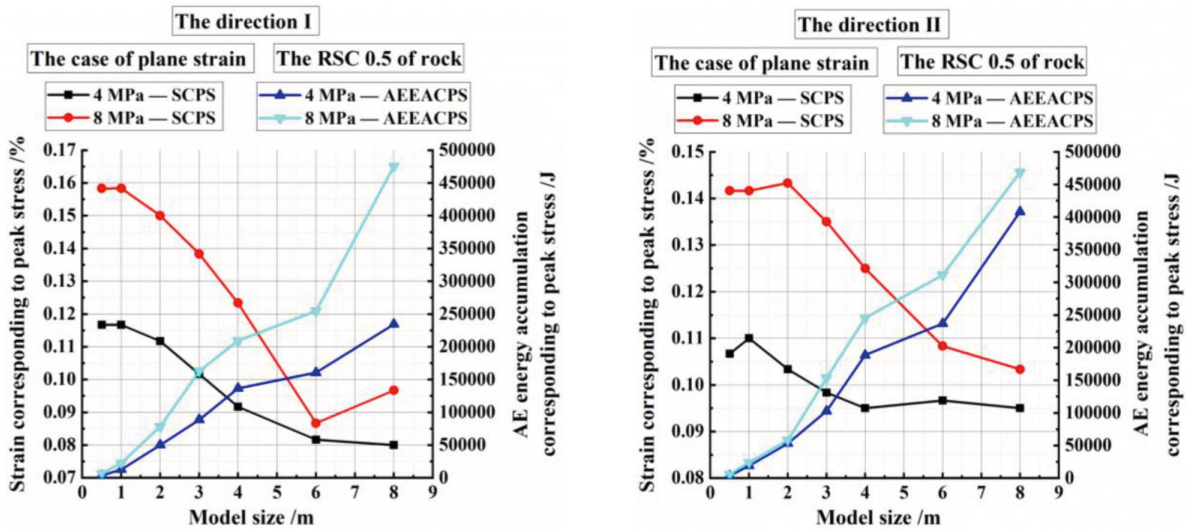

Figure 23: The strains and AE energy accumulations corresponding to peak stresses of the CJBs with different model sizes under plane strain.

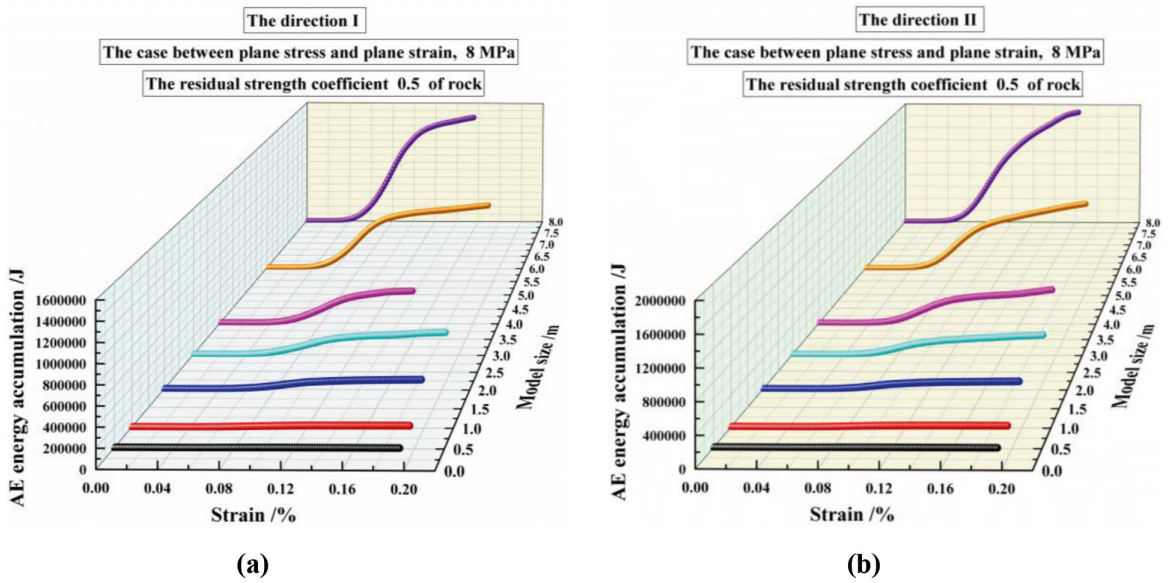

Figure 24: The AE energy accumulations of the CJBs with different model sizes under the case between plane stress and plane strain.

the mechanical behaviors of specimens in various stages were not proposed or investigated, and the influence of the rock meso-constitutive model and lateral pressure was not further considered. Stavrou et al. [40] presented the failure patterns of microdefected rocks for different lateral pressures and model sizes using the DEM, but the failure characteristics in several stages were not displayed or described in detail. Yang et al. [42] captured the fracture mode, seepage pathway, and stress field of jointed rocks with different sizes. However, the variation in rock meso-constitutive relation was not taken into account in their research. Yu et al. [45] conducted a numerical study and obtained the fracturing process of inclusions embedded in rock matrix, but the failure evolutions corresponding to different stages of stress–strain relation ships were not displayed systematically.

4.3. Influence of Rock Meso-Constitutive Relation and Model Size on AEs of Rock Mass under Lateral Pressure. Based on the results of this paper, the influence of rock meso-constitutive relation and model size on the AEs of rock mass under lateral pressure can be summarized as follows: when the model size is 4 m and the lateral pressure is 4 or 8 MPa along direction II orthogonal to the column axis, the strain

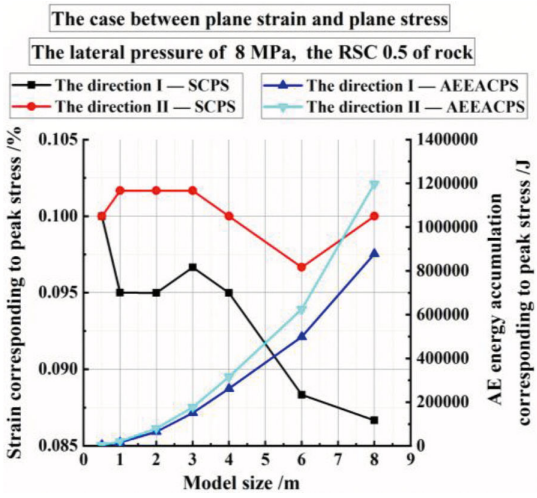

Figure 25: The strains and AE energy accumulations corresponding to the peak stresses of the CJBs with different model sizes under the case between plane stress and plane strain.

and AE energy accumulation corresponding to the peak stress first increase slightly and then rise quickly. As the model size increases, the strain that corresponds to the peak stress changes slowly at first, then decreases, and after that varies slightly, but the AE energy accumulation corresponding to the peak stress displays a trend of rising gradually.

Fan et al. [38] adopted the PFC3D method to conduct numerical simulations on jointed rock masses. However, the AE energy and the influence of the rock meso-constitutive relation on it were not further investigated. Based on a synthetic rock mass approach, Gao et al. [44] captured the variations in the microcrack number and axial stress as the axial strain increases, but further data analyses (e.g., finding the AE energy accumulation that corresponds to the peak stress or an effect analysis of model size) were not performed. Using the RFPA method, Liang et al. [46] conducted numerical simulations on jointed rock masses and presented the AE figures for their specimens, but the AE energy accumulation underlying the failure process of the specimen and the influence of the rock meso-constitutive model on it were not displayed or analyzed. Stavrou et al. [40] applied DEM to capture the fracture patterns of microdefected rocks. However, the crack-induced AE energy evolution and the influence of model size on it were not investigated deeply in their research. Based on the 3D DEM method, Ma et al. [47] obtained the typical fracture pattern of stochastic rock masses of various sizes, but the influence of the rock meso-constitutive relation on the AE energy evolution was not studied. Using the DIC technique and an AE device, Dong et al. [48] presented the features of the strains, AEs, and damage of rock media containing joints. Nevertheless, the AE energy accumulation that corresponds to the peak stress and the effect of model size were not considered. Cui et al. [49] adopted the jointed finite element technique to study the structural effect of the equivalent elastic modulus of CJRM. However, the influence of the rock meso-constitutive relation and the model size on the AE energy accumulation were not investigated in detail in their research.

5. Conclusions

Based on the continuous media mechanics and the statistical damage strength theory, a group of nonuniform CJB models with different rock meso-constitutive relations and model sizes was established. The strength and deformation properties of CJBs subject to various boundary conditions under lateral pressure, along directions I and II orthogonal to the column axis, were studied. Furthermore, the multistage mechanical and damage behavior and the evolution of the AE energy of CJBs with different rock meso-constitutive relations and model sizes under lateral pressure were investigated. Then, the strains and AE energy accumulations corresponding to peak stresses were analyzed. The main conclusions can be summarized as follows:

(1) In terms of rock RSC, the CS of CJBs increased, and the EDM of CJBs decreased or increased slightly with an increase in the rock RSC. Furthermore, the CS of CJBs slightly decreased at first and then varied slightly with an increase in the model size, while the EDM of CJBs fluctuated, but the variation was relatively small. The CS and EDM of CJBs under plane strain were relatively high in comparison with those of CJBs under the case between plane stress and plane strain, which was mainly due to the strong constraints of plane strain on CJBs.

(2) When the model size was 4 m, the rock RSC was 0.1, and the lateral pressure was 8 MPa along direction I orthogonal to the column axis, there were two obvious stages (stages I and II) to the stress–strain curve; when the rock RSC was 0.5 or 1, there were three stages (stages I, II, and III) to the stress–strain curves. When the model size was 8 m and the rock RSC was 0.1 or 0.5, there were only two obvious stages (stages I and II) to the stress–strain curves; when the rock RSC was 1, there were three different stages (stages I, II, and III) to the stress–strain curve. This phenomenon was because the plastic deformation capacity of the rock meso-elements was enhanced with the growth of the RSC, and the overall bearing capacity of CJBs was therefore improved.

(3) When the model size was 4 m and the lateral pressure was 4 or 8 MPa along direction II orthogonal to the column axis under plane strain, the strain and AE energy accumulation corresponding to the peak stress first increased slightly and then rose quickly with an increase in the rock RSC. The reason was that with the growth of rock RSC, the energy stored in and released by CJBs

becomes greater. With a growth in the model size, the strain that corresponded to the peak stress changed slowly at first, then decreased quickly, and after that, varied slightly, but the energy accumulation of the AE corresponding to the peak stress rose gradually. These results demonstrated that with the growth of the model size, the bearing capacity of CJBs decreased, and the instability precursor occurred easier.

(4) For the CJBs along direction I under the case between plane stress and plane strain, the strain corresponding to the peak stress dropped at first, then grew slightly, and then decreased with an increase in the model size. Regarding the CJBs along direction II, the strain corresponding to the peak stress fluctuated. The different changing trends were caused by the different damage development processes affected by the joint directions. Additionally, the AE energy accumulation corresponding to the peak stress rose gradually as the model size increased.

Data Availability

The datasets generated and/or analyzed during the current study are available from the corresponding author upon reasonable request.

Conflicts of Interest

The authors declare no conflicts of interest.

Authors' Contributions

Conceptualization, Yongyi Wang and Bin Gong; Data curation, Xiaoyu Yang; Formal analysis, Yongyi Wang and Xiaoyu Yang; Funding acquisition, Bin Gong; Software, Chun'an Tang; Supervision, Bin Gong and Chun'an Tang; Visualization, Yongyi Wang; Writing – original draft, Yongyi Wang; Writing – review & editing, Bin Gong. All authors have read and agreed to the published version of the manuscript.

Acknowledgments

This research was funded by the National Natural Science Foundation of China (grant number 42102314) and the China Postdoctoral Science Foundation (grant number 2020 M680950), for which the authors are very grateful.

References

[1] J. Xu, H. Li, Q. Meng, et al., "A study on triaxial unloading test of columnar-jointed-rock-mass-like material with AW velocity analysis," *Advances in Civil Engineering*, vol. 2020, December, pp. 1–14, 2020.

[2] J. X. Dou, M. X. Zhou, and Z. L. Wang, "Case study: In situ experimental investigation on overburden consolidation grouting for columnar jointed basalt dam foundation," *Geofluids*, vol. 2020, February, pp. 1–18, 2020.

[3] Z. C. Cheng, H. L. Wang, W. Y. Xu, and L. Yan, "Numerical investigation of the flow characteristics and permeability of 2D irregular columnar jointed rock masses," *Engineering Computations*, vol. 38, no. 10, pp. 4091–4110, 2021.

[4] J. Zhang, S. Pei, X. Xu, H. Li, and X. Hao, "Insights into unloading relaxation mechanism of columnar jointed basalt at the Baihetan left dam foundation," *Advances in Materials Science and Engineering*, vol. 2021, April, pp. 1–13, 2021.

[5] Z. Z. Liang, B. Gong, C. A. Tang, Y. B. Zhang, and T. H. Ma, "Displacement back analysis for a high slope of the dagangshan hydroelectric power station based on BP neural network and particle swarm optimization," *The Scientific World Journal*, vol. 2014, 2014.

[6] Q. X. Meng, H. L. Wang, W. Y. Xu, and Y. L. Chen, "Numerical homogenization study on the effects of columnar jointed structure on the mechanical properties of rock mass," *International Journal of Rock Mechanics and Mining Sciences*, vol. 124, December, p. 104127, 2019.

[7] Y. He, Z. Zhu, W. Lu, et al., "Experimental study on seepage anisotropy of a hexagonal columnar jointed rock mass," *Shock and Vibration*, vol. 2021, January, pp. 1–15, 2021.

[8] X. Xiang, L. Fan, Z. Y. Sun, G. C. Zhang, S. Zhang, and Y. H. Zhang, "Blasting relaxation characteristics of columnar jointed rock mass with AE technology," *Arabian Journal of Geosciences*, vol. 14, no. 24, p. 2827, 2021.

[9] C. Zhang, Z. Zhu, S. Wang, X. Ren, and C. Shi, "Stress wave propagation and incompatible deformation mechanisms in rock discontinuity interfaces in deep-buried tunnels," *Deep Underground Science and Engineering*, vol. 1, no. 1, pp. 25–39, 2022.

[10] W. Yao, E. Wang, X. Liu, and R. Zhou, "Fracture distribution in overburden strata induced by underground mining," *Deep Underground Science and Engineering*, vol. 1, no. 1, pp. 58–64, 2022.

[11] H. Ji, L. Yan, and J. R. Xu, "Experimental investigation on anisotropic strength and deformation behaviors of columnar jointed rock mass in confined state," *International Journal of Geomechanics*, vol. 21, no. 9, p. 06021022, 2021.

[12] W. B. Lu, Z. D. Zhu, Y. X. He, and X. C. Que, "Strength characteristics and failure mechanism of a columnar jointed rock mass under uniaxial, triaxial, and true triaxial confinement," *Rock Mechanics and Rock Engineering*, vol. 54, no. 5, pp. 2425–2439, 2021.

[13] Y. F. Wei, Q. Chen, H. Huang, and X. H. Xue, "Study on creep models and parameter inversion of columnar jointed basalt rock masses," *Engineering Geology*, vol. 290, September, p. 106206, 2021.

[14] Q. C. Sun, S. J. Li, H. S. Guo, M. Z. Zheng, and Z. Y. Yang, "In situ test of excavation damaged zone of columnar jointed rock masses under different borehole conditions," *Bulletin of Engineering Geology and the Environment*, vol. 80, no. 4, pp. 2991–3007, 2021.

[15] Q. Jiang, B. Wang, X.-T. Feng, et al., "In situ failure investigation and time-dependent damage test for columnar jointed basalt at the Baihetan left dam foundation," *Bulletin of*

Engineering Geology and the Environment, vol. 78, no. 6, pp. 3875–3890, 2019.

[16] T. Zhang, W. Y. Xu, H. L. Wang, R. B. Wang, L. Yan, and M. T. Hu, "Anisotropic mechanical behaviour of columnar jointed rock masses subjected to cyclic loading: An experimental investigation," *International Journal of Rock Mechanics and Mining Sciences*, vol. 148, December, p. 104954, 2021.

[17] Z. D. Zhu, W. B. Lu, Y. X. He, and X. C. Que, "Experimental study on the strength failure characteristics of columnar jointed rock masses under three-dimensional stress," *KSCE Journal of Civil Engineering*, vol. 25, no. 7, pp. 2411–2425, 2021.

[18] Y. He, Z. Zhu, W. Lu, et al., "Seepage flow properties of a columnar jointed rock mass in a true triaxial experiment," *Geofluids*, vol. 2021, August, pp. 1–18, 2021.

[19] J. Yu, Q. Zhang, W. Y. Xu, R. B. Wang, and H. Zhang, "Study on unloading relaxation characteristics of columnar jointed rock masses based on displacement back analysis," *Frontiers in Earth Science*, vol. 9, p. 779537, 2021.

[20] B. Gong, Y. Y. Wang, T. Zhao, C. A. Tang, X. Y. Yang, and T. T. Chen, "AE energy evolution during CJB fracture affected by rock heterogeneity and column irregularity under lateral pressure," *Geomatics, Natural Hazards and Risk*, vol. 13, no. 1, pp. 877–907, 2022.

[21] Y. Y. Wang, B. Gong, C. A. Tang, and T. Zhao, "Numerical study on size effect and anisotropy of columnar jointed basalts under uniaxial compression," *Bulletin of Engineering Geology and the Environment*, vol. 81, no. 1, p. 41, 2022.

[22] J. C. Zhang, Q. Jiang, X. J. Hao, et al., "Analysis of stress-structural collapse mechanism of columnar jointed basalt under high stress," *Rock and Soil Mechanics*, vol. 42, no. 9, pp. 2556–2568, 2021.

[23] G. Li, K. Wang, B. Gong, Z. Tao, K. Du, and C. Tang, "A multi-temporal series high-accuracy numerical manifold method for transient thermoelastic fracture problems," *International Journal of Solids and Structures*, vols. 230–231, November, 2021.

[24] C. A. Tang and S. Q. Kou, "Crack propagation and coalescence in brittle materials under compression," *Engineering Fracture Mechanics*, vol. 61, nos. 3–4, pp. 311–324, 1998.

[25] Z. Z. Liang, D. K. Xiao, C. C. Li, X. K. Wu, and B. Gong, "Numerical study on strength and failure modes of rock mass with discontinuous joints," *Chinese Journal of Geotechnical Engineering*, vol. 36, no. 11, pp. 2086–2095, 2014.

[26] T. T. Chen, G. R. Foulger, C. A. Tang, S. A. Mathias, and B. Gong, "Numerical investigation on origin and evolution of polygonal cracks on rock surfaces," *Engineering Geology*, vol. 311, December, p. 106913, 2022.

[27] T. Xu, P. G. Ranjith, P. L. P. Wasantha, J. Zhao, C. A. Tang, and W. C. Zhu, "Influence of the geometry of partially-spanning joints on mechanical properties of rock in uniaxial compression," *Engineering Geology*, vol. 167, December, pp. 134–147, 2013.

[28] Y. Wang, B. Gong, Y. Zhang, X. Yang, and C. Tang, "Progressive fracture behavior and acoustic emission release of CJBs affected by joint distance ratio," *Mathematics*, vol. 10, no. 21, p. 4149, 2022.

[29] X. H. Feng, B. Gong, C. A. Tang, and T. Zhao, "Study on the non-linear deformation and failure characteristics of EPS concrete based on CT-scanned structure modelling and cloud computing," *Engineering Fracture Mechanics*, vol. 261, February, 2022.

[30] X. Z. Liu, C. A. Tang, L. C. Li, P. F. Lv, and H. Y. Liu, "Microseismic monitoring and 3D finite element analysis of the right bank slope, Dagangshan hydropower station, during reservoir impounding," *Rock Mechanics and Rock Engineering*, vol. 50, pp. 1901–1917, 2017.

[31] J. R. Zhou, J. Wei, T. H. Yang, W. C. Zhu, L. C. Li, and P. H. Zhang, "Damage analysis of rock mass coupling joints, water and microseismicity," *Tunnelling and Underground Space Technology*, vol. 71, January, pp. 366–381, 2018.

[32] X. H. Feng, B. Gong, X. F. Cheng, H. H. Zhang, and C. A. Tang, "Anisotropy and microcrack-induced failure precursor of shales under dynamic splitting," *Geomatics, Natural Hazards and Risk*, vol. 13, no. 1, pp. 2864–2889, 2022.

[33] B. P. Chen, B. Gong, S. Y. Wang, and C. A. Tang, "Research on zonal disintegration characteristics and failure mechanisms of deep tunnel in jointed rock mass with strength reduction method," *Mathematics*, vol. 10, no. 6, p. 922, 2022.

[34] J. Mazars and G. Pijaudier-Cabot, "Continuum damage theory—application to concrete," *Journal of Engineering Mechanics*, vol. 115, no. 2, pp. 345–365, 1989.

[35] Z. Q. Ke, H. L. Wang, W. Y. Xu, Z. N. Lin, and H. Ji, "Experimental study of mechanical behaviour of artificial columnar jointed rock mass containing transverse joints," *Rock and Soil Mechanics*, vol. 40, no. 2, pp. 660–667, 2019.

[36] W. Weibull, "A statistical distribution function of wide applicability," *Journal of Applied Mechanics*, vol. 18, no. 3, pp. 293–297, 1951.

[37] M. Mahboubi Niazmandi and S. M. Binesh, "A DFN–DEM approach to study the influence of confinement on the REV size of fractured rock masses," *Iranian Journal of Science and Technology, Transactions of Civil Engineering*, vol. 44, no. S1, pp. 587–601, 2020.

[38] X. Fan, P. H. S. W. Kulatilake, and X. Chen, "Mechanical behavior of rock-like jointed blocks with multi-non-persistent joints under uniaxial loading: A particle mechanics approach," *Engineering Geology*, vol. 190, May, pp. 17–32, 2015.

[39] X. B. Liu, S. H. He, and D. H. Wang, "Numerical analysis of the anisotropy and scale effects on the strength characteristics of defected rockmass," *Advances in Civil Engineering*, vol. 2020, February, pp. 1–21, 2020.

[40] A. Stavrou and W. Murphy, "Quantifying the effects of scale and heterogeneity on the confined strength of micro-defected rocks," *International Journal of Rock Mechanics and Mining Sciences*, vol. 102, February, pp. 131–143, 2018.

[41] Q. Wu and P. H. S. W. Kulatilake, "REV and its properties on fracture system and mechanical properties, and an orthotropic constitutive model for a jointed rock mass in a dam site in China," *Computers and Geotechnics*, vol. 43, June, pp. 124–142, 2012.

[42] T. Yang, H. Y. Liu, and C. A. Tang, "Scale effect in macroscopic permeability of jointed rock mass using a coupled stress–damage–flow method," *Engineering Geology*, vol. 228, October, pp. 121–136, 2017.

[43] Y. Y. Wang, B. Gong, and C. A. Tang, "Numerical investigation on anisotropy and shape effect of mechanical properties of columnar jointed basalts containing transverse joints,"

Rock Mechanics and Rock Engineering, vol. 55, no. 11, pp. 7191–7222, 2022.

[44] F. Q. Gao, D. Stead, and H. P. Kang, "Numerical investigation of the scale effect and anisotropy in the strength and deformability of coal," *International Journal of Coal Geology*, vol. 136, pp. 25–37, 2014.

[45] C. Y. Yu, B. Gong, N. Wu, P. L. Xu, and X. K. Bao, "Simulation of the fracturing process of inclusions embedded in rock matrix under compression," *Applied Sciences*, vol. 12, no. 16, p. 8041, 2022.

[46] Z. Z. Liang, N. Wu, Y. C. Li, H. Li, and W. R. Li, "Numerical study on anisotropy of the representative elementary volume of strength and deformability of jointed rock masses," *Rock Mechanics and Rock Engineering*, vol. 52, no. 11, pp. 4387–4402, 2019.

[47] C. Ma, W. M. Yao, Y. Yao, and J. Li, "Simulating strength parameters and size effect of stochastic jointed rock mass using DEM method," *KSCE Journal of Civil Engineering*, vol. 22, no. 12, pp. 4872–4881, 2018.

[48] T. Dong, P. Cao, Q. Lin, et al., "Size effect on mechanical properties of rock-like materials with three joints," *Geotechnical and Geological Engineering*, vol. 38, no. 4, pp. 4073–4089, 2020.

[49] Z. Cui, Q. Sheng, and X. L. Leng, "Study on structural effect of equivalent elastic modulus of columnar jointed rock mass," in *Proceedings of the 2015 3rd International Conference on Machinery, Materials and Information Technology Applications*, W. Du and X. Zhou, Eds., pp. 1599–1607, Atlantis Press, 2015.